

Star formation efficiency across large-scale galactic environments

Laya Ghodsi^{1,2*}, Allison Man¹, Darko Donevski^{3,4}, Romeel Davé^{5,6,7}, Seunghwan Lim⁸, Christopher C. Lovell^{9,10}, Desika Narayanan^{11,12}

¹ Department of Physics & Astronomy, University of British Columbia, 6224 Agricultural Road, Vancouver BC, V6T 1Z1, Canada

² ESO, Karl Schwarzschild strasse 2, 85748 Garching, Germany

³ National Centre for Nuclear Research, Pasteura 7, 02-093 Warsaw, Poland

⁴ SISSA, Via Bonomea 265, 34136 Trieste, Italy

⁵ Institute for Astronomy, University of Edinburgh, Royal Observatory, Blackford Hill, Edinburgh, EH9 3HJ, United Kingdom

⁶ University of the Western Cape, Bellville, Cape Town 7535, South Africa

⁷ South African Astronomical Observatories, Observatory, Cape Town 7925, South Africa

⁸ Canadian Institute for Theoretical Astrophysics, University of Toronto, 60 St. George St., Toronto, ON M5S 3H4, Canada

⁹ Institute of Cosmology and Gravitation, University of Portsmouth, Burnaby Road, Portsmouth, PO1 3FX, United Kingdom

¹⁰ Astronomy Centre, University of Sussex, Falmer, Brighton BN1 9QH, United Kingdom

¹¹ Department of Astronomy, University of Florida, 211 Bryant Space Sciences Center, Gainesville, FL 32611 USA

¹² Cosmic Dawn Center (DAWN), Niels Bohr Institute, University of Copenhagen, Jagtvej 128, København N, DK-2200, Denmark

6 September 2023

ABSTRACT

Environmental effects on the formation and evolution of galaxies have been one of the leading questions in galaxy studies during the past few decades. In this work, we investigate the relationship between the star formation activity of galaxies and their environmental matter density using the cosmological hydrodynamic simulation SIMBA. The galactic star formation activity indicators that we explore include the star formation efficiency (SFE), specific star formation rate (sSFR) and molecular hydrogen mass fraction ($f_{\text{H}_2}^*$) and the environment is considered as the large scale environmental matter density, calculated based on the stellar mass of nearby galaxies on a 1 Mpc/h grid using the cloud in cell (CIC) method. Our sample includes galaxies with $9 < \log \frac{M_*}{M_\odot} < 11$, divided into three stellar mass bins to disentangle the effects of stellar mass and environment on the star formation activity of galaxies. For low- to intermediate-mass galaxies at low-redshifts ($z < 1.5$), we find that the star formation efficiency of those in high-density regions are ~ 0.3 dex lower than those in low-density regions. However, there is no significant environmental dependence of the star formation efficiency for massive galaxies over all our redshift range, and low- to intermediate-mass galaxies at high redshifts ($z > 1.5$). We present a scaling relation for the depletion time of cold molecular hydrogen ($t_{\text{depl}} = 1/\text{SFE}$) as a function of galaxy parameters including environmental density. Our findings provide a framework for quantifying the environmental effects on the star formation activities of galaxies as a function of stellar mass and redshift. The most significant environmental dependence is seen at later cosmic times ($z < 1.5$) and towards lower stellar masses ($9 < \log \frac{M_*}{M_\odot} < 10$). Future large galaxy surveys can use this framework to look for the environmental dependence of the star formation activity and examine our predictions.

Key words: Galaxy formation and evolution, Star formation, Molecular gas, Depletion time, Hydrodynamic simulation

1 INTRODUCTION

It is well established that the environment of galaxies affects their properties including colour (Balogh et al. 2004; Bamford et al. 2009), morphology (Dressler 1980; Goto et al. 2003; Skibba et al. 2009) and star formation rate (SFR; Kauffmann et al. 2004; Peng et al. 2010; Woo et al. 2013; Old et al. 2020). These works show that in the low-redshift universe ($z < 1$), galaxies in dense regions tend to

be redder, more elliptical, and less star-forming. In contrast to the low-redshift universe, there is no consensus in the literature about the relationship between SFR and the environment at high redshift ($z > 1$). Some studies claim that at high redshift, galaxies in dense regions have higher SFRs than galaxies in low-density regions, on average (Elbaz et al. 2007; Cooper et al. 2008; Santos et al. 2014, 2015; Shimakawa et al. 2018). This suggested change in the relationship between SFR and the environment at roughly $z \sim 1$ is called the reversal of the SFR-density relation. This trend partially arises from the virialization process of galaxy clusters. The overdense regions in

* E-mail: Layaghodsi@phas.ubc.ca

the low-redshift universe are mostly virialized galaxy clusters subject to physical processes including starvation and ram pressure stripping that can reduce the star formation activity of the member galaxies. Whereas, the overdense regions in the higher-redshift universe are mostly non-virialized protoclusters and have large intergalactic gas reservoirs to fuel the star formation in galaxies. However, other observational and theoretical studies find no evidence for a relationship between SFR and the environment of galaxies (Scoville et al. 2013; Darvish et al. 2016; Duivenvoorden et al. 2016; Lovell et al. 2021) or find the same relationship as the low-redshift universe (Patel et al. 2009). Observational studies on this topic suffer from selection biases due to observational limits that restrict the sample redshift and stellar mass ranges and different methods to define and measure environments and galaxy properties (Muldrew et al. 2012, 2015; Lovell et al. 2018). Exploring this research question using hydrodynamic simulations helps in understanding the background physics of galaxy formation and evolution producing the observed trends (Yajima et al. 2022). Although simulations also suffer from known limitations, they have been able to predict many observational trends. For instance, Tonnesen & Cen (2014) and Hwang et al. (2019) have been able to reproduce the reversal of SFR-density relation using hydrodynamic simulations up to redshifts $z = 1$ and $z = 2$, respectively.

Cold molecular gas, mainly consisting of molecular hydrogen, is the star formation fuel in galaxies. Studying the effects of the environment on the molecular hydrogen content is thus essential to dissect the role of the environment on the star formation activity of galaxies. Observational studies find different trends for the role of the environment on galactic molecular gas content. At low-redshift, a few studies find no correlation between the environment and the molecular gas content of galaxies (Kenney & Young 1989; Lavezzi & Dickey 1998; Koyama et al. 2017). However, some works report that molecular gas content increases with the environmental density (Mok et al. 2016) while others report that molecular gas content decreases with environmental density (Fumagalli et al. 2009; Scott et al. 2013; Boselli et al. 2014). Molecular gas observations for high-redshift galaxies ($z > 1.5$) are currently quite limited in sample sizes and affected by selection biases. Nevertheless, Some works at this redshift range find higher gas fractions for cluster galaxies than the field galaxies (Noble et al. 2017; Hayashi et al. 2018), while other works find no environmental dependence for gas fraction (Lee et al. 2017; Tadaki et al. 2019).

Since SFR and molecular hydrogen content, two tracers for galactic star formation activity, are correlated, it is useful to define another parameter that relates these two parameters to trace the variations of SFR and molecular hydrogen mass at the same time. Star formation efficiency (SFE) is typically defined as the SFR per molecular hydrogen mass ($\text{SFE} \equiv \text{SFR}/M_{\text{H}_2}$; Young et al. 1996; Boselli et al. 2001). Similarly, depletion time ($t_{\text{depl}} = 1/\text{SFE} = M_{\text{H}_2}/\text{SFR}$) is the timescale during which the galaxy converts all of its molecular hydrogen into new stars at the current star formation rate. A fall in SFR could be due to a lower molecular hydrogen mass supply, and/or less efficient star formation. It is thus important to monitor these three galactic star formation activity parameters together to gain a comprehensive understanding of galaxy evolution (Scoville et al. 2017; Lu et al. 2022).

Previous studies have tried to quantify the SFE and gas depletion time as functions of other galaxy properties. Scoville et al. (2017) quantified the gas depletion time as a function of redshift, star formation rate, and stellar mass. Similarly, Tacconi et al. (2018) introduced a scaling relation for the depletion time as a function of redshift, star formation rate, stellar mass, and the radius of galaxies. These works, however, lack the environmental effects on galactic star formation

activity. Darvish et al. (2018b) includes a number of environmental indicators to the Scoville et al. (2017) scaling relation, but they do not find an environmental dependence of the gas depletion time in their sample of galaxies with $\log \frac{M_*}{M_\odot} > 10$ at $0.5 < z < 3.5$. It is worth mentioning that most of the known scaling relations are for star-forming galaxies in the field, without explicit measurements of the environment they reside in (Tacconi et al. 2018; Liu et al. 2019). Systematic investigations of the star formation efficiency of galaxies versus the environment remain sparse to date.

To derive more complete knowledge of galaxy gas properties, we must also investigate whether galaxy large-scale environment regulates the link between the gas and star formation. The environment of galaxies is defined in a variety of ways based on the available data set and the goal of different studies. On large scales, the matter content in the Universe is distributed in a web-like structure, called the cosmic web. This structure consists of dense massive nodes, long filaments connecting the nodes, vast thin walls, and huge low-density regions called voids. Some works define the environment of galaxies as the cosmic web component in which the galaxy resides (Hahn et al. 2007; Moorman et al. 2016; Xu et al. 2020). However, the complexity of this structure and the wide range of different physical definitions for the components of the cosmic web makes it complicated to study the environmental effects on galaxies using this environment tracer. In addition, membership in a galaxy cluster or field is another definition for galactic environment (Vulcani et al. 2013; Zavala et al. 2019; Lemaux et al. 2020). The result of studies using this method is a strong function of the definition of cluster/field galaxies for which there is not a consensus in the community. At high redshift ($z > 2$), this environment measure is even more tricky given the lack of massive virialized galaxy clusters. Moreover, this dichotomy does not cover the full dynamic range of different galactic environments. The environmental density of galaxies is another measure of the environment. As summarized in Muldrew et al. (2012) and Etherington & Thomas (2015), two commonly used methods in the literature to measure environmental density include: (i) the density within a volume around the galaxy determined by the distance between the galaxy and its N^{th} nearest neighbour, where N typically ranges from 5 to 10 (Bamford et al. 2009; Ellison et al. 2010; Wu 2020). (ii) the density within a cell, sphere, or cylinder around the galaxy determined by a fixed aperture (Berrier et al. 2011; Smolčić et al. 2017). These methods are computationally fast to perform. The results of these methods might be functions of N for the first method and the fixed aperture size for the second method. The nearest neighbour-based methods probes the internal trends of massive halos better, while the fixed aperture-based method is a better probe for scales larger than individual halos (Muldrew et al. 2012). Variations of the last two methods use two/three-dimensional measures and number/luminosity/mass density which makes the comparison of different studies on this topic even more complicated and tricky. Moreover, the peculiar motion of galaxies along the line of sight, leading to the Kaiser effect (finger of god), makes it complicated to measure the exact densities (Kaiser 1987). The reader can refer to Haas et al. (2012), Muldrew et al. (2012), and Darvish et al. (2015) for a more detailed discussion about different environment indicators.

In this study, we use the environmental density as an environment indicator calculated considering the stellar mass of neighbour galaxies on a $1 \text{ h}^{-1} \text{ Mpc}$ grid. An advantage of using this method over using the number density of galaxies as an environment measure is that the stellar mass density in the vicinity of a galaxy can be directly linked to the luminosity density of neighbour galaxies on the same scale which is measurable from observations. Moreover, stellar mass density captures the underlying matter distribution better than num-

ber density which is susceptible to stochastic effects. Furthermore, in both observations and simulations, the uncertainties in mass density are smaller than that in number density since small galaxies that are difficult to detect in data or resolve in simulations are large in number but small in mass (Tonnesen & Cen 2014).

Although observational capabilities have significantly advanced recently, their ability to detect faint galaxies is still limited by the sensitivity of the instrument. Hence, observed galaxy catalogues, specifically at high redshift, are not complete and suffer from selection biases. This limitation, in addition to various approaches used to measure galactic properties from observations, makes it difficult to capture bias-free trends in galaxy properties. Using simulations is a fruitful method to model galaxies theoretically, avoid observational selection biases, and explore the physical processes that drive the observed trends. In this work, using a set of simulated galaxies from the SIMBA hydrodynamic cosmological simulation (Davé et al. 2019), we aim to shed new light on a question: Does the environment of galaxies affect their star formation activity? We investigate the galactic star formation activity parameters, including SFE, sSFR, molecular hydrogen mass fraction, and depletion time, as functions of redshift, stellar mass, and environmental density. The data set used spans a relatively wide redshift range ($0 < z < 4$), wide stellar mass range ($9 < \log \frac{M_*}{M_\odot} < 13$), wide environmental density range ($-4 < \log [1 + \delta_{\text{gal}}^*] < 2$), and a large number of galaxies ($\sim 330,000$ galaxies). The environmental density is calculated using the stellar mass density of neighbour galaxies on a 1 Mpc/h grid, calculated using the Cloud in Cell (CIC) method.

This paper is structured as follows: section 2 presents the properties of the SIMBA simulation and the data we use. In section 3, we explain our methods to calculate the environmental density and error propagation. In section 4 we present our results. Section 5 discusses the results and possible interpretations. Finally, section 6 summarises the main findings of the work.

2 THE SIMBA SIMULATION

In this work, we study the environmental dependence of the star formation activity of galaxies in SIMBA, a state-of-art cosmological hydrodynamic simulation. In this section, we briefly explain the main methods and physical prescriptions used to derive the galaxy properties in this simulation.

SIMBA (Davé et al. 2019) is a suite of galaxy formation and evolution simulations in a cosmological context built on the MUFASA project (Davé et al. 2016) with updated physics for the modelling of black hole growth and feedback. SIMBA uses the meshless finite mass version of the GIZMO code (Hopkins 2015), assuming the Planck Collaboration et al. (2016) cosmological parameters of $\Omega_m = 0.3$, $\Omega_\Lambda = 0.7$, $\Omega_b = 0.048$, $H_0 = 68 \text{ km s}^{-1} \text{ Mpc}^{-1}$, $\sigma_8 = 0.82$, $n_s = 0.97$, and the star formation model of Schmidt (1959). This simulation explores the evolution of galaxies, black holes, and galactic gas over a wide redshift range. The molecular hydrogen content in SIMBA is calculated on the fly using the prescription provided in Krumholz & Gnedin (2011) based on the local gas metallicity and column density as follows:

$$f_{H_2} = 1 - 0.75 \frac{s}{1 + 0.25s} \quad (1)$$

Where f_{H_2} is the molecular hydrogen mass fraction (mass of molecular hydrogen over the total gas mass of each gas cell) for each gas cell and s is defined as

$$s = \frac{\ln(1 + 0.6\chi + 0.01\chi^2)}{0.0396Z(\Sigma/M_\odot \text{ pc}^{-2})} \quad (2)$$

Where Z is the metallicity in solar units. The gas column density (Σ) needs to be estimated using the Sobolev (Sobolev 1960) approximation as $\Sigma = \rho h$ where ρ is the mass density of gas and h is the local density scale height in each gas cell in the simulation box, to be computed using $h = \rho/|\nabla\rho|$. In this equation, χ is a function of metallicity, defined as

$$\chi \approx 3.1 \left(\frac{1 + 3.1Z^{0.365}}{4.1} \right) \quad (3)$$

Having the molecular hydrogen mass fraction from the above equations, one can calculate the number density of molecular hydrogen n_{H_2} in each gas cell.

Stars only form in gas cells with $n_H > 0.13 \text{ cm}^{-3}$. The star formation rate (SFR) in each star-forming gas cell is calculated using the molecular hydrogen mass fraction f_{H_2} , gas mass density ρ , and dynamical timescale t_{dyn} with the Schmidt (1959) star formation model as $SFR = \epsilon_* f_{H_2} \rho / t_{\text{dyn}}$, assuming the star formation efficiency per free-fall time to be $\epsilon_* = 0.02$ (Robert C. Kennicutt 1998). Galactic SFR values are instantaneous and calculated by summing over gas cells. These values are also consistent with the SFRs calculated using young stellar particles, averaged over tens of Myr. SIMBA finds galaxies by applying a 6-dimensional Friends-of-Friends (6DFoF) galaxy finder on all stars and gas cells with $n_H > 0.13 \text{ cm}^{-3}$. Halos are found using a 3DFoF method applied on dark matter particles with a linking length set to 0.2 times the mean interparticle spacing.

SIMBA models the star formation-driven galactic winds as decoupled two-phase winds with 30% of the particles consisting of hot particles. The scaling relation of the mass loading factor with stellar mass comes from Anglés-Alcázar et al. (2017b) using the FIRE simulation (Hopkins et al. 2014). One of the main improvements of SIMBA compared to MUFASA is that black holes are seeded and grown on the fly and the feedback from black hole accretion contributes to galaxy quenching. SIMBA has two black hole accretion modes; torque-limited accretion for cold gas within the black hole ($T < 10^5 \text{ K}$) using the model of Anglés-Alcázar et al. (2017a) based on Hopkins & Quataert (2011), and Bondi accretion (Bondi 1952) for hot gas ($T > 10^5 \text{ K}$). The active galactic nuclei (AGN) feedback in SIMBA includes X-ray energy feedback based on the model of Choi et al. (2012) and a kinetic subgrid model consisting of radiative and jet modes. The radiative mode is used for high Eddington ratios ($f_{\text{Edd}} = \dot{M}_{\text{BH}}/\dot{M}_{\text{Edd}} > 0.2$) when multi-phase winds of molecular and warm ionized gas flow from AGNs with a speed of roughly 10^3 km s^{-1} . The jet mode feedback begins to be implemented at lower Eddington ratios ($f_{\text{Edd}} < 0.2$) and only becomes dominant at $f_{\text{Edd}} < 0.02$. In this feedback mode, AGNs produce collimated jets of hot gas with a speed of roughly 10^4 km s^{-1} . Additionally, these jets only exist in early-type galaxies with black hole mass of $M_{\text{BH}} > M_{\text{BH,lim}} = 10^{7.5} M_\odot$ to be consistent with observations. The velocities and temperatures of the bipolar kinetic feedback model are mostly taken from observation to reproduce the observed energy release on larger scales of tens of kpc (Davé et al. 2019). The jet mode AGN feedback has been shown to be the main mechanism responsible for galaxy quenching in SIMBA. The X-ray mode feedback is the complementary process to fully quench galaxies. However, the radiative mode does not contribute to galaxy quenching (Davé et al. 2019).

SIMBA considers the galaxy stellar mass function (GSMF) as a test for its feedback model since the GSMF is well measured over a

reasonable redshift range (Davé et al. 2019). Assuming the observed GSMF from Bernardi et al. (2017), the combined CANDELS and zFOURGE data from Tomczak et al. (2014), and CANDELS data from Song et al. (2016), SIMBA has a GSMF in good agreement with these observations with the exception of a subtle overproduction of massive galaxies at $z < 2$. This inconsistency of the GSMF of massive galaxies between SIMBA and observations could be due to a number of observational biases or numeric uncertainties in SIMBA (Davé et al. 2019): first, the massive end of GSMF could be underestimated in observations, which arises from missing massive dusty galaxies in the considered rest-frame optical surveys. Second, the most massive galaxies have bottom-heavy initial mass functions (IMF with a larger ratio of low-mass stars with $M < M_\odot$ compared to Milky Way-like galaxies; Conroy et al. 2013). This may cause an underestimation of the stellar masses of most massive galaxies in observations. Third, the most massive simulated galactic systems usually have extended envelopes of stars and satellites around them that might be overmerged into the main central part of the galaxy because of poor resolution. As a result, the stellar mass of a fraction of these galaxies might be overestimated in simulations. Moreover, the SIMBA run used in this work with a box length of $100 h^{-1}\text{Mpc}$ produces a halo with a virial mass of $M_{\text{halo}} = 1.16 \times 10^{15} M_\odot$ by $z = 0$ as its largest halo. However, this halo is 50% more massive than expected for this volume. This may contribute to the overproduction of massive galaxies in SIMBA. If galaxies in SIMBA are found using a fixed aperture of 30 kpc (similar to the EAGLE simulation; Schaye et al. 2015), the GSMF would be in significantly better agreement with observations.

In this work, we use 22 snapshots of the SIMBA full run simulation (m100n1024) over the redshift range of $0 < z < 4$. This simulation has been run in a box of $100 h^{-1}\text{Mpc}$ in length with 1024^3 gas particles and 1024^3 dark matter particles. The minimum gravitational softening length is $0.5 h^{-1}\text{kpc}$. In this run, the gas particle mass, the dark matter particle mass, and the minimum stellar mass of a resolved galaxy are $1.82 \times 10^7 M_\odot$, $9.6 \times 10^7 M_\odot$, and $5.8 \times 10^8 M_\odot$ respectively. We apply a lower stellar mass limit of $M_* > 10^9 M_\odot$ on our galaxy sample at all analyzed redshifts, which is the same as the lower mass limit of the sample that Tacconi et al. (2018) uses to find scaling relations between galaxy molecular gas masses, stellar masses, and star formation rates. Assuming this limit, we can compare our results with this scaling relation.

3 METHODS

In this section, we explain the methods used to investigate the effect of the environment on the star formation activity of galaxies. To achieve our goal, we study a number of important parameters in the star formation process of galaxies:

- Specific star formation rate ($sSFR = SFR/M_*$, unit $[\text{yr}^{-1}]$): The rate of forming new stars per stellar mass.
- Molecular hydrogen fraction ($f_{\text{H}_2}^* = M_{\text{H}_2}/M_*$): The mass fraction of the molecular hydrogen compared to stellar mass.
- Star formation efficiency (SFE, unit $[\text{yr}^{-1}]$): The efficiency of producing new stars in a galaxy, also the inverse of the time a galaxy takes to consume all of its molecular gas to form new stars (t_{depl}):

$$\text{SFE} = sSFR/f_{\text{H}_2}^* = SFR/M_{\text{H}_2} = 1/t_{\text{depl}} \quad (4)$$

Having these quantities from the simulation, we need an environment indicator to explore the relationship between the star formation process in galaxies and their large-scale environment.

3.1 Stellar mass density as an environment indicator

Among the various existing methods of measuring the environment of galaxies, we decided to investigate the relation between the stellar mass environmental density of the neighbour galaxies and the star formation activity of each galaxy. Stellar mass density is a good indicator of the large-scale environment of galaxies and traces the underlying matter distribution in the Universe, therefore giving more intrinsic environmental trends. (Mo & White 1996; Wang et al. 2018). We also performed our analysis using the number density of neighbour galaxies that resulted in the same trends, but weaker. In this study, we calculate the stellar mass density by considering the stellar mass of each galaxy and all of its neighbour galaxies in a $1 h^{-1}\text{Mpc}$ grid. We choose $1 h^{-1}\text{Mpc}$ for our grid size because it represents the typical size of virialized galaxy clusters, so it is large enough to capture the super-halo environmental trends (Kauffmann et al. 2004; Muldrew et al. 2012). The general trends reported in this work remain the same when changing this parameter by a few megaparsecs. Our mass interpolation method is the Cloud In Cell (CIC) method that gives a fraction of the weight of each particle to all vertices of the cell it occupies (Birdsall & Fuss 1969). This method reduces density measurement errors compared to other mass assignment schemes. The dimensionless quantity environmental density (also known as overdensity or density contrast) is defined with the following equation:

$$\delta_{\text{gal}}^*(x) = (\rho(x) - \bar{\rho}) / \bar{\rho} \quad (5)$$

Where $\rho(x)$ is the stellar mass density of galaxies in 3-dimensional space at point x and $\bar{\rho}$ is the mean stellar mass density of the simulation box. Pylians3¹ (Villaescusa-Navarro et al. 2018) is our tool for this calculation which is a set of python libraries, written in Python, Cython and C to facilitate the analysis of numerical simulations. We use the defined environmental density (δ_{gal}^*) as an indicator of the environment in this work. The results of this work remain the same if we consider dark matter mass rather than stellar mass density.

3.2 Error and scatter estimation

We use the median as a statistical tool to investigate the overall evolution of $sSFR$, $f_{\text{H}_2}^*$, and SFE with galaxy properties including stellar mass, redshift, and environmental density. The median is chosen as the statistical indicator of our data sample because it is robust against outliers and false measurements. In order to capture the entire behaviour of the data, we need to look at the measurement error of our statistical indicator and scatter of the data as well.

We use bootstrapping to measure the error of the median of $sSFR$, $f_{\text{H}_2}^*$, and SFE for our analysis. Bootstrapping is a resampling method useful for estimating bias and variance. In order to calculate a function in a data set with N data points using bootstrapping, the first step is to generate B new data sets ($B=10000$ in our case) from the original data set each of size N with replacement. Then one can calculate the function on each new data set and keep track of the statistical distribution of these values.

Furthermore, we need to quantify how the data points are scattered around the median values to avoid extracting trends only from median values. We use median absolute deviation (MAD) for measuring the scatter of data points around the median values. The MAD is defined

¹ <https://pylians3.readthedocs.io/en/master/>

as the median of the absolute deviations from the median of the data for a data set X_1, X_2, \dots, X_n :

$$MAD = \text{median}(|X_i - \text{median}(X_i)|) \quad (6)$$

In our case, data points X_i can be the sSFR, $f_{\text{H}_2}^*$, and SFE of each galaxy with index i .

4 RESULTS

In the previous sections, we defined our galaxy sample, our methods, and the important parameters to investigate including specific star formation rate (sSFR), molecular hydrogen mass fraction ($f_{\text{H}_2}^*$), star formation efficiency (SFE) of galaxies, and environmental density (δ_{gal}^*). In the remainder of the paper, we present and interpret our results based on galaxy evolution theories and other works on this topic, focusing on our central question: "What is the effect of the Mpc-scale environment on the star formation activity of galaxies?"

4.1 The redshift evolution of star formation efficiency across galactic environments

In this subsection, we present the trends we detect between sSFR, $f_{\text{H}_2}^*$, SFE, and environmental density of galaxies in the SIMBA simulation. Figure 1 presents the median star formation efficiency, median specific star formation rate and the median molecular hydrogen mass fraction of galaxies as functions of the environmental density (as defined in section 3.1) in the redshift range of $0 < z < 4$ in the top row. We only show eight redshift snapshots in this figure for visual clarity. The star formation efficiency is shown in the top left panel of Figure 1, indicating that at high redshifts ($z > 1$) galaxies in denser regions form stars more efficiently than galaxies in low-density regions, for instance by ~ 0.2 dex at $z = 4$. However, at lower redshifts ($z < 1$) galaxies in denser regions form stars less efficiently than galaxies in low-density regions, for instance by ~ 0.25 dex at $z = 0$.

Investigating the environmental density dependence of the specific star formation rate and the molecular hydrogen mass fraction is insightful to interpret the visible trends for SFE. The top middle panel of Figure 1 presents the median sSFR values for galaxies as a function of the environmental density for different redshift snapshots. At high redshifts ($z > 1$), the sSFR-density curves are almost flat on average, with subtle variations in the densest bins. The slope of the curves becomes negative towards lower redshift ($z < 1$), meaning that at these redshifts galaxies in denser regions have lower sSFR values compared to galaxies in low-density regions, for example by ~ 0.9 dex at $z = 0$. Finally, the top right panel of Figure 1 shows the environmental density dependence of the molecular hydrogen mass fraction of galaxies at different redshift snapshots. This plot shows that the molecular hydrogen mass fraction of galaxies decreases with environmental density at all redshifts by ~ 0.2 for $z = 4$ and ~ 0.15 for $z = 0$.

Considering all of the trends shown in Figure 1, one can see that at high redshift ($z > 1$), the increase of SFE with environmental density arises from the decrease of $f_{\text{H}_2}^*$ with environmental density. However, at low redshift ($z < 1$), the decrease of sSFR with environmental density seems to be stronger than the decrease of $f_{\text{H}_2}^*$ with environmental density, leading the $\text{SFE} = \text{sSFR}/f_{\text{H}_2}^*$ to decrease with environmental density as well. Overall, the slope of the $\text{SFE} - \delta_{\text{gal}}^*$ curves is negative at low redshifts ($z < 1$) and positive at high redshifts ($z > 1$). We can call this change in the slope of the $\text{SFE} - \delta_{\text{gal}}^*$

at $z \sim 1$ a "reversal" of SFE-density relation (analogous to the reversal of SFR-density relation introduced in Elbaz et al. 2007; Popesso et al. 2015).

The bottom row of Figure 1 presents the median absolute deviation (MAD) of SFE, sSFR, and the molecular hydrogen mass fraction versus the environmental density of galaxies with different colours indicating the different explored redshifts. MAD is a measure of the scatter in the data. The scatter of galaxy sSFR, plotted in the bottom middle panel of Figure 1, increases with environmental density at all redshift snapshots. We think it results from high galactic activity in dense regions, including merger and AGN feedback, compared to lower-density regions. However, the scatters of SFE and $f_{\text{H}_2}^*$ do not directly depend on the environmental density.

In order to investigate the reversal of the SFE-density relation, we look at the redshift evolution of the SFE-density relation directly in Figure 2. These plots show SFE, sSFR, and $f_{\text{H}_2}^*$ as functions of redshift for different overdensities, shown by different colours. The redshift evolution of SFE is plotted in the left panel of Figure 2, suggesting a reversal of SFE-density relation around $z \sim 1$. At high redshift ($z = 4$), galaxies in dense regions form stars more efficiently than galaxies in low-density regions by ~ 0.3 dex. While in the local universe ($z = 0$), galaxies in dense regions form stars less efficiently than those in low-density regions by ~ 0.3 dex.

The top right panel of Figure 2 shows that in the high-redshift universe in SIMBA ($z \sim 4$), galaxies in denser regions (darker curves) have slightly higher median sSFR (~ 0.2 dex) than galaxies in low-density regions (lighter curves). However, this trend changes at lower redshifts in a way that at $z \sim 0$, galaxies in high-density regions have much lower median sSFR (~ 0.9 dex) than galaxies in low-density regions. Based on this panel, one can argue that we have a reversal of the sSFR-density relation with a turning point around $z \sim 2.5$. The drop in the sSFR-redshift curves occurs earlier in more dense regions. Hence, this reversal in the sSFR-density relation reflects that galaxy quenching happens earlier in high-density regions compared to low-density regions. The bottom right panel of Figure 2 shows the redshift evolution of the molecular hydrogen mass fraction for different environment densities. From this plot, it is clear that galaxies in the two densest bins on average have larger molecular hydrogen mass fractions at high redshift compared to the low-redshift snapshots. The same trend can be seen for galaxies in low-density regions after a certain redshift. Furthermore, galaxies in denser regions have a lower molecular hydrogen mass fraction compared to those in low-density regions at all redshifts. Consequently, the reversal of SFE-density relation mainly arises from the redshift evolution of sSFR.

4.2 Redshift evolution of SFE-density relation: Environment or mass dependency?

We detect an environmental dependence for the redshift evolution of the star formation activity of galaxies in Figure 2. However, environmental density may just be one of the many factors affecting the star formation activity of galaxies. According to observed scaling relations, other factors like the stellar mass of galaxies may also affect their star formation efficiency (Peng et al. 2010). Moreover, the correlation between massive galaxies and dense environments may bias the interpretation of environmental trends (Bolzonella et al. 2010; Darvish et al. 2015; Bahé et al. 2017). Furthermore, If an environmental dependence persists after controlling for stellar mass, we can conclude that the environment is indeed one factor leading to the trends reported in the last section. In this section, we divide our galaxy sample into three stellar mass bins in order to distinguish

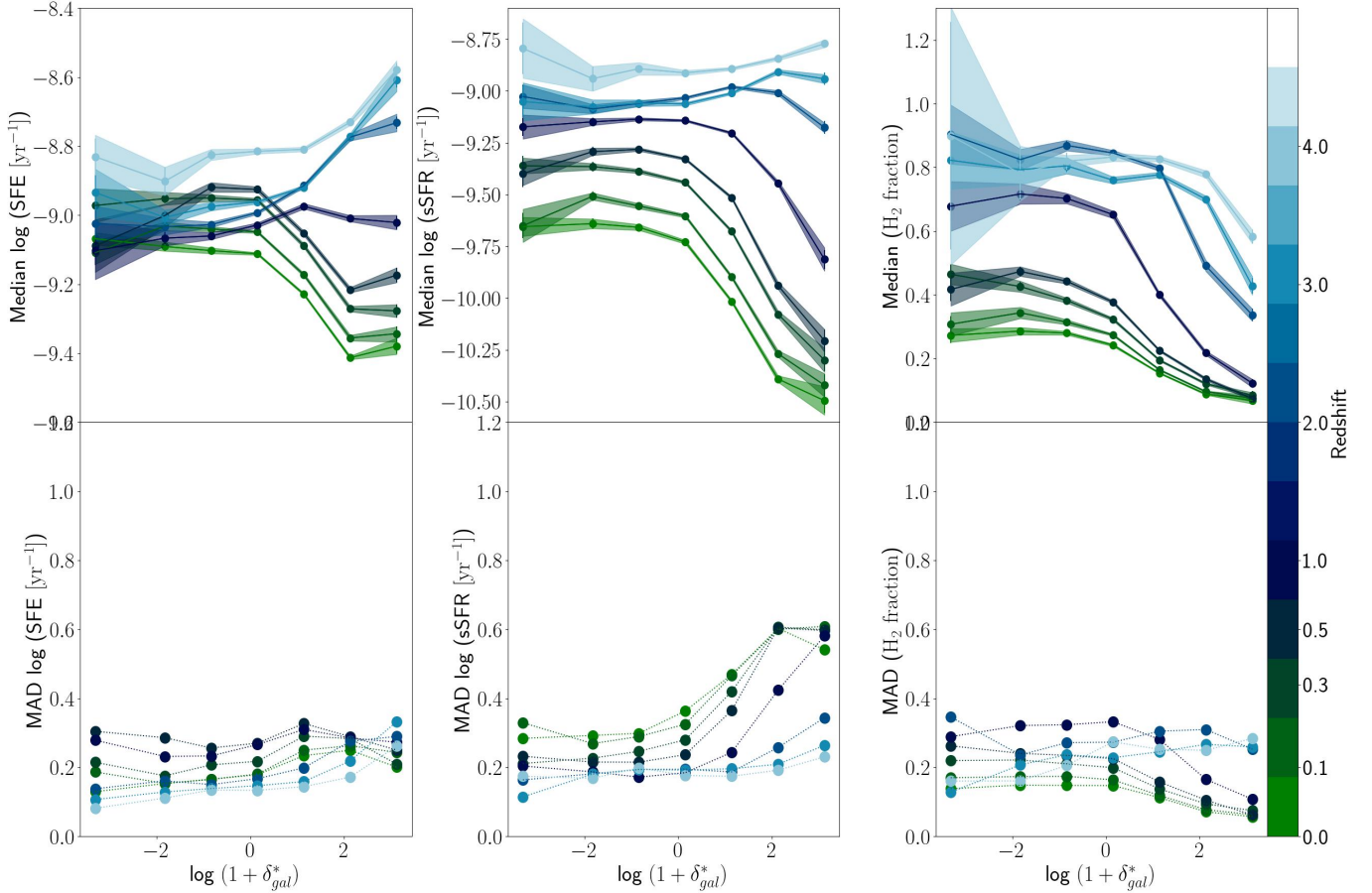


Figure 1. Top left: Median galactic SFE(= $\text{sSFR}/f_{\text{H}_2}^*$) as a function of the environmental density, δ_{gal}^* , at different redshifts, shown by the colour bar. Green colours show the present day at $z = 0$. In each environmental density bin, the median values and their uncertainties (shaded areas) are obtained from bootstrapping. Top middle: similar to the left panel for sSFR (= SFR/M_*) versus environmental density. Top right: Same as the top left panel for the molecular hydrogen mass fraction $f_{\text{H}_2}^*$ (= M_{H_2}/M_*) versus environmental density. Bottom row: Median Absolute Deviation (MAD) of galaxy SFE, sSFR, and $f_{\text{H}_2}^*$ versus environmental density at different redshifts. The slope of the SFE-density curve is changing by redshift, showing the reversal of SFE-density relation.

between the effect of mass and the effect of the environment on the star formation activity of galaxies.

Figure 3 shows the dependence of the SFE, sSFR, and the molecular hydrogen mass fraction of galaxies on the environmental density for different redshifts and galaxy stellar masses. Each column in this figure demonstrates galaxy properties in a specific stellar mass bin, starting from galaxies with $9 < \log \frac{M_*}{M_\odot} < 9.5$ in the left column, to galaxies with $9.5 < \log \frac{M_*}{M_\odot} < 10$ in the middle column, and galaxies with $10 < \log \frac{M_*}{M_\odot}$ in the right column. We have 3 stellar mass bins, 22 redshift bins, and 5 environmental density bins, generating 330 data points in each row of Figure 3. The detailed information on the number of galaxies in each bin is provided in Table A1.

The top row panels of Figure 3 explore the redshift evolution of SFE. In the top left and top middle panels (low- and intermediate-mass bins) we can see that for the galaxies in the local universe ($z \sim 0$), those in denser regions have ~ 0.3 dex lower SFE values than those in low-density regions. However, we do not see a significant dependence on the environmental density for low- and intermediate-mass galaxies in the high redshift universe. Furthermore, the effect of the environmental density on the SFE of massive galaxies (top right panel) is much less prominent than in lower-mass galaxies. In fact, only galaxies in the densest bin have ~ 0.2 dex higher SFE than

other galaxies at $z = 0$. Comparing the top row of Figure 3 with the left panel of Figure 2, we can see that at $z \sim 4$, the visible trend in Figure 2 is not an effect of the environmental density, but it mainly arises from the large range of SFE values in different mass bins. The overall trend in the low-redshift universe ($z < 1$) of Figure 2 is seen in the low and intermediate-mass bins of Figure 3, but not in its most massive bin. Hence, the environmental density has a small effect on the star formation efficiency of low- and intermediate-mass galaxies in the low-redshift universe.

The middle row of Figure 3 presents the redshift evolution of sSFR. Similar to the SFE plots in the top row, an environmental density dependence of sSFR in the local universe ($z \sim 0$) is noticeable (~ 0.5 dex) in the low- and intermediate-stellar mass galaxies. However, these low- and intermediate-mass galaxies do not show a density dependence of their sSFR in the high redshift universe ($z \sim 4$). For the most massive galaxies, an environmental dependence is only discernible between redshifts $z \sim 1$ and $z \sim 3$. At this redshift range, galaxies in denser regions have lower sSFR values than those in low-density regions. There is no obvious trend seen for these galaxies in the local universe ($z \sim 0$) or the highest redshift bins ($z > 3$). By comparing the middle row of Figure 3 with the top right panel of Figure 2, one can argue that the overall trend at the

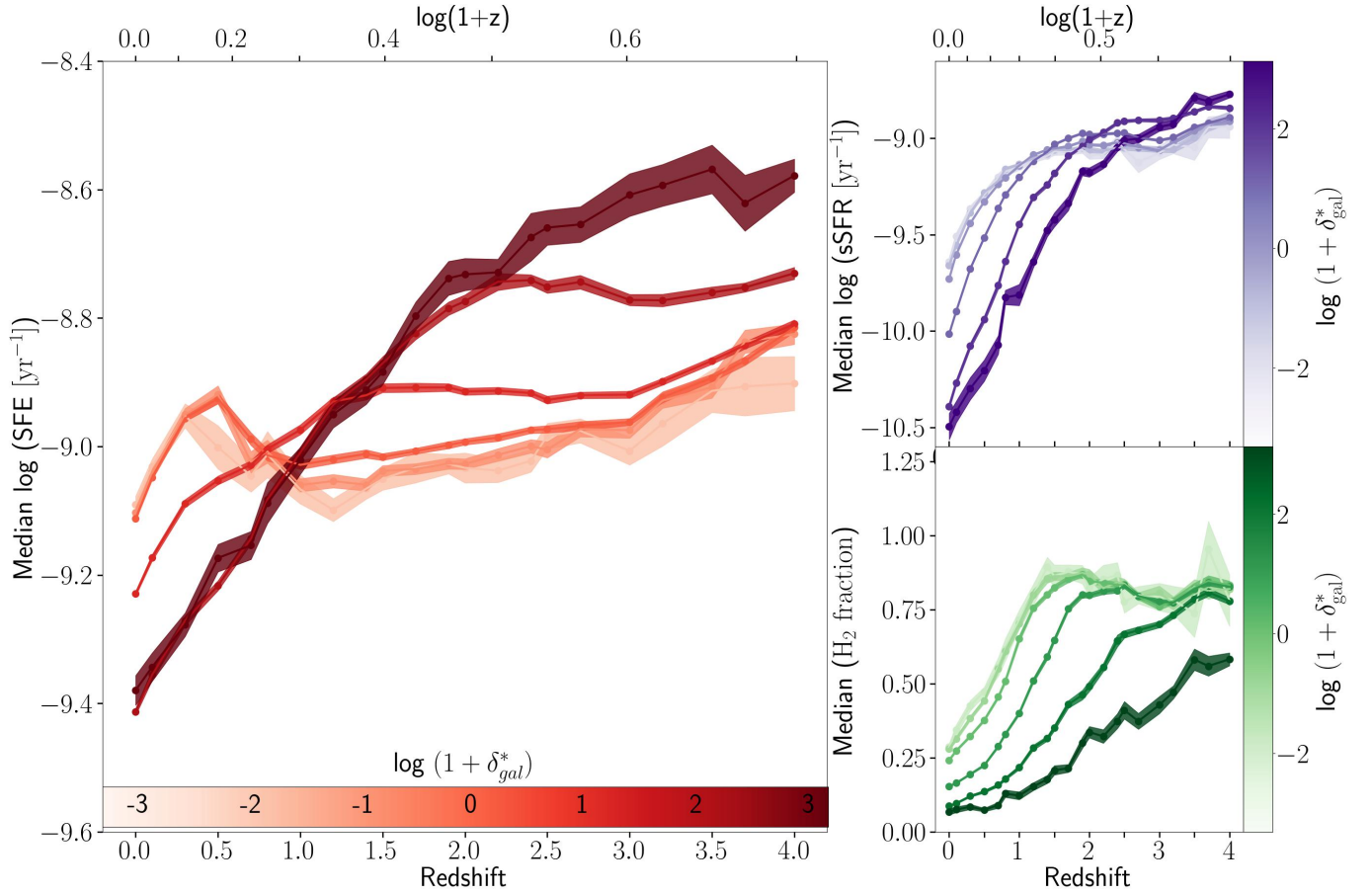


Figure 2. SFE, sSFR, and molecular hydrogen mass fraction as functions of redshift for different environmental densities, shown by colours. The reversal point of the SFE-density and sSFR-density relations are at $z \sim 1$ and $z \sim 2.5$, respectively.

local universe ($z \sim 0$) is primarily driven by lower-mass galaxies ($9 < \log \frac{M_*}{M_\odot} < 10$).

The redshift evolution of molecular hydrogen mass fraction is illustrated in the bottom row of Figure 3 for galaxies at different stellar mass bins, and environment overdensities. The most significant trend in these plots is that all galaxies in the densest bins have the lowest hydrogen mass fraction at almost all redshifts explored in this work ($0 < z < 4$). Moreover, more massive galaxies have lower hydrogen fractions, on average, which is consistent with the trend seen in [Davé et al. \(2020\)](#). The molecular hydrogen mass fraction shows the most prominent dependence on environmental density, more than that of the sSFR and the SFE (Figures 2 and 3).

In conclusion, our analysis shows a slight dependence of the star formation efficiency of galaxies in SIMBA at low- to intermediate-mass bins ($9 < \log \frac{M_*}{M_\odot} < 10$) at low-redshifts ($z < 1.5$). However, we do not detect a reversal of SFE-density relation in Figure 3 in each mass bin, meaning that this is a pure effect of the stellar mass of galaxies and not their environment.

4.3 Scaling relations for gas depletion time

We fit scaling relations to the galaxy parameters to examine the statistical significance of the trends observed in Figures 2 and 3. [Tacconi et al. \(2018\)](#) fits the depletion time (t_{depl}) as a function of redshift (z), specific star formation rate (sSFR), stellar mass (M_*),

and galaxy’s half-light radius (R_h) in the rest frame optical band 5000 Å with the following equation which we refer to as the PHIBSS scaling relation (Plateau de Bure High- z Blue Sequence Survey²) in this work:

$$\log t_{\text{depl}}(\text{Gyr}) = A_t + B_t \log(1+z) + C_t \log(\delta MS) + D_t (\log M_* - 10.7) + E_t \log(\delta R_h) \quad (7)$$

Where $\delta MS = sSFR/sSFR_{(MS,z,M_*)}$ in which $sSFR_{(MS,z,M_*)}$ is the specific star formation rate of the star-forming main sequence galaxies, defined in [Speagle et al. \(2014\)](#) with the following equations:

$$\log \frac{sSFR_{(MS,z,M_*)}}{\text{Gyr}^{-1}} = 9 - (6.51 - 0.11 \times \frac{t_c}{\text{Gyr}}) + (-0.16 - 0.026 \times \frac{t_c}{\text{Gyr}}) \times (\log \frac{M_*}{M_\odot} + 0.025) \quad (8)$$

Where

$$\log \frac{t_c}{\text{Gyr}} = 1.143 - 1.026 \times \log(1+z) - 0.599 \times \log^2(1+z) + 0.528 \times \log^3(1+z) \quad (9)$$

Furthermore, $\delta R_h = R_h/R_{h0}(z, M_*)$, where $R_{h0}(z, M_*)$ is the average half-light radius of the star-forming

² <https://www.iram.fr/phibss2/Home.html>

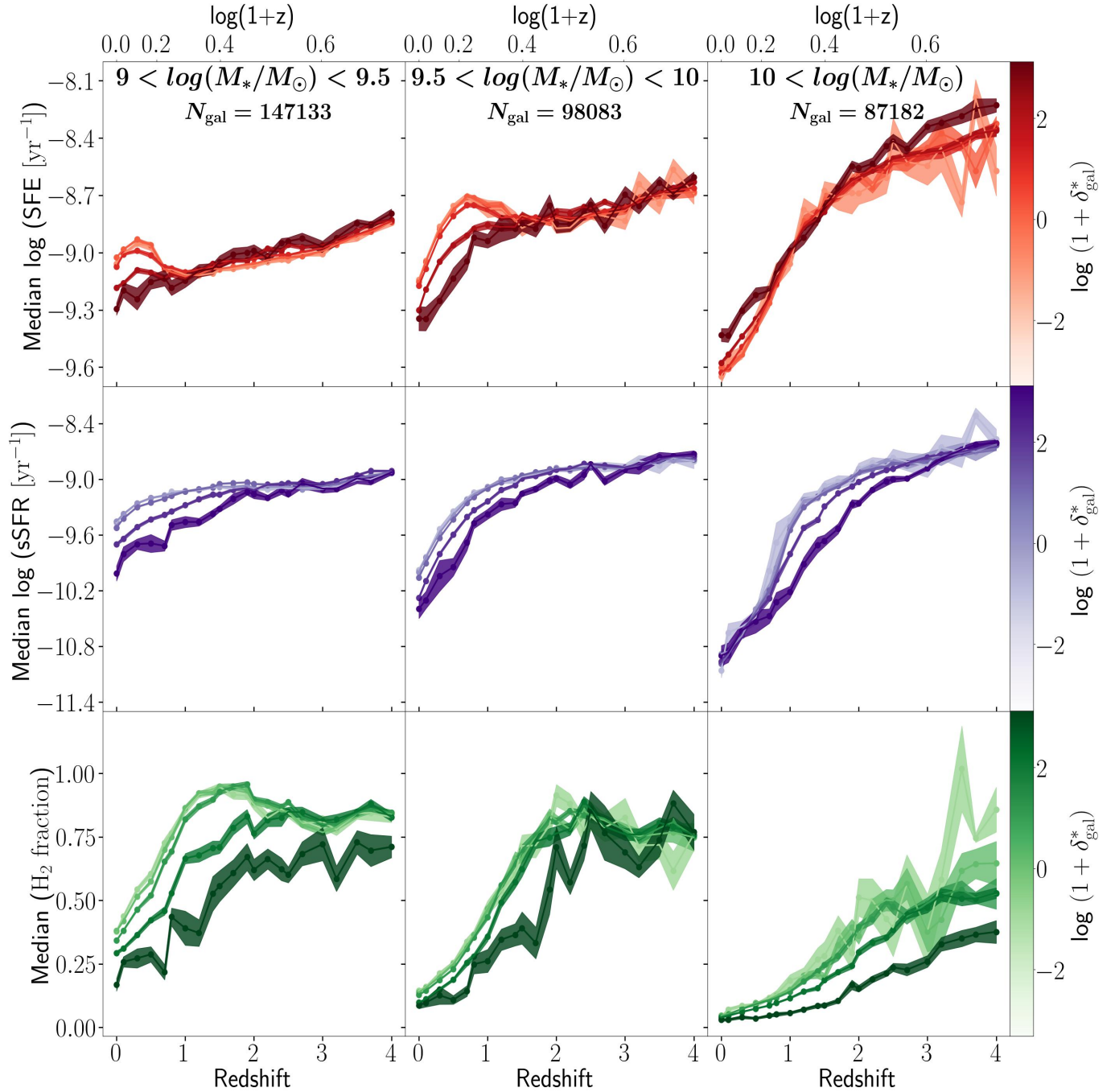


Figure 3. *Top:* Median SFE as a function of redshift for different stellar masses and environment overdensities, calculated using bootstrapping as described in section 3.2. Each column shows a stellar mass bin and colours represent the environmental density bin. Error bars show the standard deviation of bootstrapped median values. *Middle:* Same as the top row, but for the specific star formation rate (sSFR). *Bottom:* Same as the top row for molecular hydrogen mass fraction $f_{\text{H}_2}^*$. The environmental dependence of SFE is mostly prominent for low- and intermediate-mass galaxies at low redshift.

population, defined in van der Wel et al. (2014) as $R_{\text{e}0} = 8.9 \text{ kpc} (1+z)^{-0.75} (M_*/5 \times 10^{10} M_{\odot})^{0.23}$.

Tacconi et al. (2018) fits Equation 7 to the PHIBBS survey, consisting of a large sample of 1444 star-forming galaxies in the redshift range of $0 < z < 4$, a stellar mass range of $9 < \log \frac{M_*}{M_{\odot}} < 11.8$, and the star formation rate relative to the main sequence in range of $10^{1.3} < \delta \text{MS} < 10^{2.2}$. The overall best-fit parameters are:

$$A_t = +0.09, \quad B_t = -0.62, \quad C_t = -0.44, \\ D_t = +0.09, \quad E_t = +0.11$$

Krumholz & Dekel (2012); Hunt et al. (2016) argue that metallicity affects the star formation activity of galaxies as well. Following this idea, we include this parameter in our study on SIMBA. In this work, we modified Equation 7 to include two additional terms to fit for the

environmental density and the galaxy mass-weighted metallicity:

$$\log t_{\text{depl}} (\text{Gyr}) = A + B \log(1+z) + C \log sSFR + D \log M_* + E \log(R_h) + F \log(Z) + G \log(1 + \delta_{\text{gal}}^*) \quad (10)$$

We evaluate the significance of each term by performing linear regression to ten slightly different variations of Equation 10. As summarized in Table A2, the first six models exclude either the environment factor or gas metallicity. Models 7 to 10 include both of them, and some use δMS instead of $sSFR$ and some use δR_h instead of R_h . The R^2 value, the so-called "coefficient of determination", ranges between 0 to 1 with higher values showing statistically better fits. The coefficients, their standard errors, their 95% confidence intervals, and their p-values are also presented for each model. The p-value shows the significance of the parameter in the fit. A p-value of less than 0.05 is considered to be statistically significant. The highest R^2 value (0.866192) belong to the 8th/10th model where we have redshift ($1+z$), specific star formation rate ($sSFR$), stellar mass (M_*), radius (R_h) or normalized size ($\delta R_h = R_h/R_{e0}(z, M_*)$), metallicity (Z), environmental density ($1 + \delta_{\text{gal}}^*$) included in the model. This evaluation shows that the environment is an important term for determining the gas depletion time of galaxies. Interestingly, using $sSFR$ gives a better fit than using δMS based on their R^2 , but using radius (R_h) or the normalized radius ($\delta R_h = R_h/R_{e0}(z, M_*)$) does not make a different. Excluding the environmental density or the metallicity leads to a (slightly) poorer fit. This is consistent with the recent observational studies, showing the environmental dependences of the gas-phase metallicity of galaxies (Chartab et al. 2021; Calabrò et al. 2022).

Figure 4 presents a comparison between the actual star formation efficiency of SIMBA galaxies, the SFE predicted by our tenth model, and the SFE predicted by the Tacconi et al. (2018) scaling relation. As expected, the environmental dependence of galactic SFE seen in SIMBA at different redshifts, stellar mass, and environmental density bins is captured in the predicted SFEs from our scaling relation. Interestingly, the SFE values predicted by the Tacconi et al. (2018) relation show an environmental dependence even though environmental density is not an explicit parameter in their scaling relation. This might be due to the environmental dependence of other fit parameters, for instance, $sSFR$ and size or simply because denser regions tend to contain more massive galaxies. Figure 5 shows a relative comparison between the actual SIMBA SFE values and the SFE predicted by our tenth scaling relation. The model is predicting the SFE values with accuracy within 30% of the actual values. The predicted values follow the general trends of our SFE-redshift curves in most of the bins.

5 DISCUSSION

Mass and environment are the two determinants suggested in the literature for the evolution of galaxies (Peng et al. 2010, 2012; Darvish et al. 2016). The effects of these factors on star formation activity have been studied from different viewpoints and using different methods. In this section, we discuss our results in the context of the literature findings.

5.1 Impact of the stellar mass on star formation

The stellar mass of a galaxy is an important indicator of its evolutionary path, including its past and ongoing star formation activity. For instance, more massive galaxies in SIMBA have more massive black holes consistent with observations (Davé et al. 2019). According to

the black hole growth model of SIMBA, the accretion rate of black holes increases with their mass (Davé et al. 2019). Therefore, galaxies with larger stellar masses and corresponding higher black hole masses have higher black hole accretion rates. Moreover, Thomas et al. (2019) show that SFR increases with the black hole accretion rate for star-forming ($SFR > 1 M_\odot \text{yr}^{-1}$) galaxies in SIMBA at redshift $0 < z < 5$. They suggest this arises from the common gas reservoir used for star formation and torque-limited black hole growth mode.

The AGN jet feedback in SIMBA is the main quenching responsible for galaxies with black hole mass $M_{\text{BH}} > 10^{7.5} M_\odot$ which corresponds to stellar mass $M_* > 10^{10} M_\odot$ (Thomas et al. 2019). Consequently, the most massive galaxies we investigate in this work are significantly affected by the AGN jet feedback which might be one of the reasons their SFE and $sSFR$ drop more rapidly than lower-mass galaxies (Figure 3). Since AGN jet particles in SIMBA are decoupled until they reach outside the galaxy (tens of kpc), they cannot directly remove gas from the interstellar medium (ISM) of the galaxy (Davé et al. 2019). However, the AGN jets in SIMBA are implemented to heat up the gas in the circumgalactic medium (CGM) of galaxies which truncates the accretion of cold gas from the CGM into the galaxy (Appleby et al. 2021). We do not investigate the impacts of AGN in this work, however, a potential trend could be as follows: since more massive galaxies tend to reside in more dense regions (Bahé et al. 2017), their strong AGN jet feedback can disturb the cooling and accretion of the CGM gas, resulting in less fuel for star formation and a drop in the SFE and $sSFR$ of these galaxies compared to those in lower-density regions (the right column of Figure 3). The faster drop of SFE and $sSFR$ of massive galaxies compared to lower mass galaxies, can partially cause the reversal of SFE-density and $sSFR$ -density relations we show in Figure 2.

It is commonly known that mass quenching is more effective on more massive galaxies at higher redshifts while environment quenching is mostly effective on lower mass galaxies at lower redshifts (Peng et al. 2010; Darvish et al. 2018a). Recent observational studies find quenched massive galaxies (with mass completeness limit of $\log M_*/M_\odot > 10 - 11$) in high redshift protoclusters ($1.4 < z < 3.3$) (Zavala et al. 2019; Alberts et al. 2022; McConachie et al. 2022; Ito et al. 2023; Mei et al. 2023). Since galaxy protoclusters are not fully virialized in this phase, the effect of environment quenching might not be as significant as the effect of mass quenching. Assuming that these recently reported protoclusters are overdense regions at the observed redshifts, they could be in line with the trends seen in Figure 3, showing that the most massive galaxies of SIMBA in dense regions have lower $sSFR$ compared to those in low-density regions at $0.5 < z < 3$.

Zavala et al. (2019) attributed the observed quenched massive galaxies in protoclusters to the early phases of environment quenching. They argue that this process is due to the environment because of the high fraction of quenched galaxies in overdense regions. They use ALMA Band 6 observations to investigate the SFE and gas fractions (defined as the ratio of the ISM gas to the total gas and stellar mass) in 68 members of two massive protoclusters at $2 < z < 2.5$. Their sample spans a stellar mass range of $9 < \log \frac{M_*}{M_\odot} < 11.6$. While they find, on average, similar scaling relations between the most massive galaxies ($\log \frac{M_*}{M_\odot} > 10$) in protoclusters and those from the field, they argue that a discernible fraction of the lower-mass galaxies might have enhanced efficiencies. Their observed trend for massive galaxies is consistent with our detected trends presented in Figure 3, showing no environmental dependence for SFE for massive galaxies. However, their low-mass galaxy sample ($\log \frac{M_*}{M_\odot} < 10$) is incomplete and cannot be used to extract any trends.

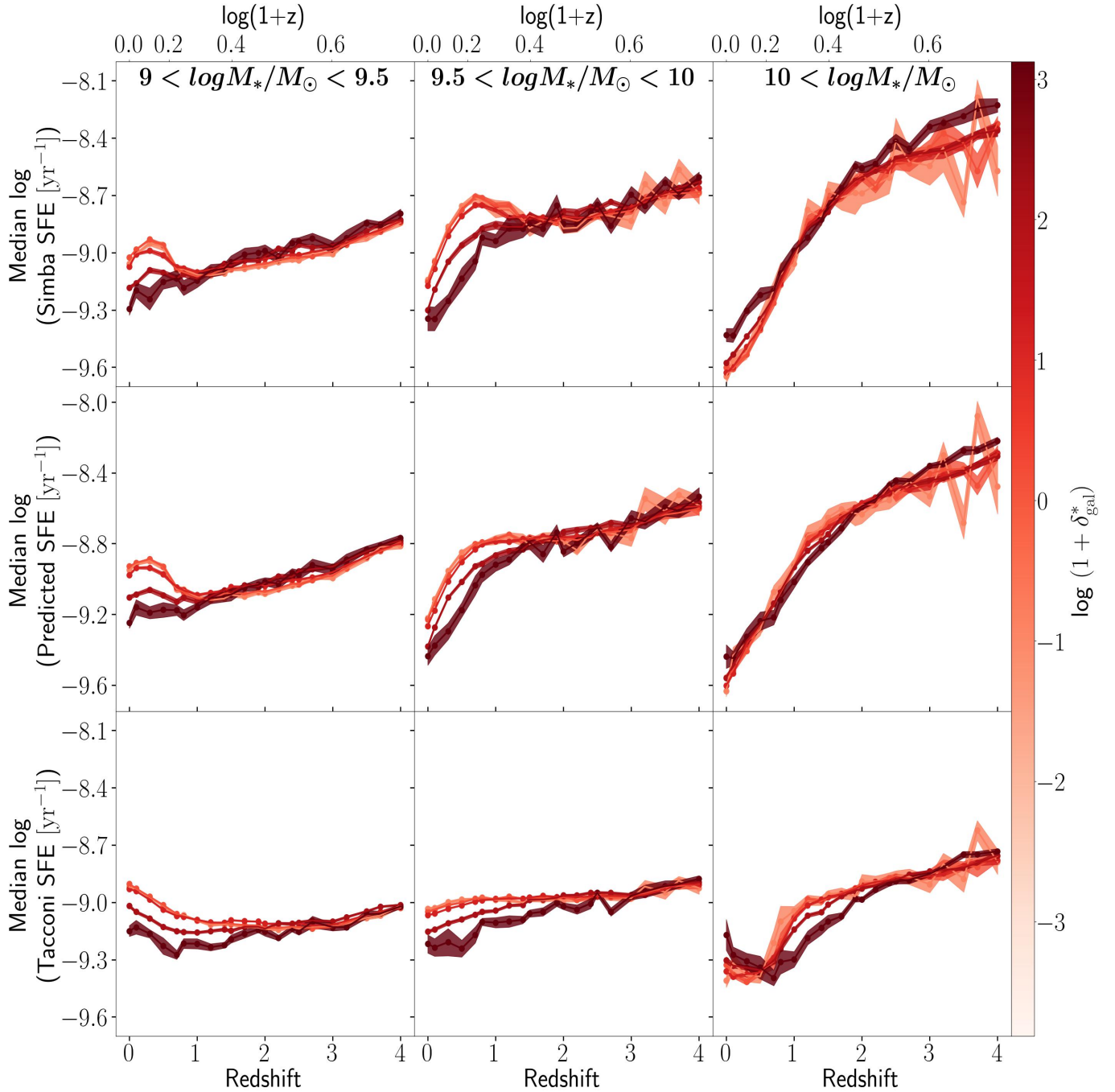


Figure 4. Cosmic evolution of SFE for galaxies with different stellar masses. *Top:* The actual SFE inferred from SIMBA. *Middle:* The SFE predicted by the best scaling relation from this work (10th model in Table A2). *Bottom:* The SFE computed from the observational scaling relation by Tacconi et al. (2018) following the procedures described in Sec 4.3. Colours show environmental density. The environmental dependence of SFE (seen in Figure 3) is reproduced using our scaling relation.

5.2 Impact of the environment on star formation

Our analysis shows that at low redshift ($z < 1.5$), lower-mass galaxies with $9 < \log \frac{M_*}{M_\odot} < 10$ in the SIMBA simulation that reside in denser regions have, on average, lower SFEs and lower sSFRs compared to galaxies in low-density regions (Figure 3). This trend has been seen in other observational and simulation works as well and

usually is attributed to environmental quenching caused by different environmental processes.

More mergers in dense regions could be a reason for environmental quenching. Rodríguez Montero et al. (2019) studies mergers and the resulting starburst and quenching at $0 < z < 2.5$ in SIMBA. They find in merger events the SFR can increase up to 2-3 times the SFR of normal star-forming galaxies. They show this jump in SFR for low-mass galaxies ($\log \frac{M_*}{M_\odot} < 10.5$) is due to the more molecular gas content in

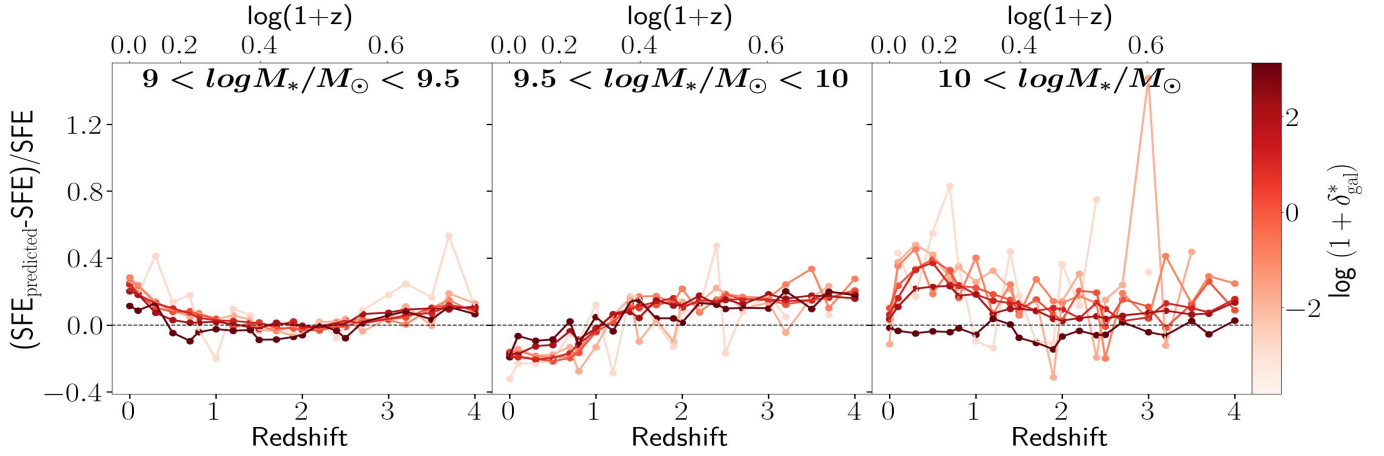


Figure 5. The relative difference of the predicted SFE using the second model (SFE as a function of z , M_* , sSFE, δ_{gal}^*) and the actual SFE values as a function of redshift for different stellar mass bins and environmental density bins. The model predictions are close to the data.

the final galaxy. While, for more massive galaxies ($\log \frac{M_*}{M_\odot} > 10.5$), this jump arises from higher SFE because of more dense molecular gas in the galaxy after the merger. Since merger events are more abundant in denser regions, this SFR jump for mergers could result in an enhancement of SFR of galaxies in denser regions, in contradiction to the trends seen in our work. However, the SFR jump caused by mergers in Rodríguez Montero et al. (2019) makes up a very little part (a couple of percent) of the overall cosmic SFR of SIMBA and its effect cannot be significantly detected. Consequently, their results are not in direct contradiction to our results.

Darvish et al. (2016) finds that the environment and mass quenching depend on each other in a way that environment quenching happens more efficiently for massive galaxies than lower mass galaxies and mass quenching occurs more efficiently in dense regions. They suggest mergers as the main cause of this finding. In this work, they investigate the relationship between the galactic environment, stellar mass, and star formation activity for 73481 galaxies in the COSMOS field in the redshift range of $0.1 < z < 3.1$. Their mass-complete galaxy sample has a K_s -band magnitude limit of $K_s < 24$ and a stellar mass range of $9.14 < \log \frac{M_*}{M_\odot} < 11.5$. They measure the SFRs and stellar masses using a spectral energy distribution (SED) template fitting to the available UV, optical, and mid-IR data. The limiting stellar mass of this data set grows with redshift, such that in the redshift range of $0.1 < z < 0.5$ the data set is complete for galaxies with stellar mass $9.14 < \log \frac{M_*}{M_\odot}$, while this limit grows to 9.97 at $1.5 < z < 3.1$. Darvish et al. (2016) uses the Voronoi tessellation method to calculate the environmental density of galaxies. This work shows that at $z < 1$ the median SFR and median sSFR decrease with increasing density, while they become independent of redshift at $z > 1$. They argue that environmental quenching is the dominant quenching process at $z < 1$. At $z > 1$, mass quenching is the dominant process that likely arises from stellar feedback.

In general, a direct and precise comparison of observations and simulations is not feasible due to the different nature of these data. Furthermore, the methods used to measure the galactic parameters, including SFR, molecular hydrogen, and environment in our work are different from Darvish et al. (2016). Nonetheless, it is still instructive to perform a qualitative comparison. Keeping these points in mind, we look at SFR and sSFR as functions of density for different redshifts in our work and Darvish et al. (2016) in Figure 6 for a qualitative comparison. We apply the same mass completeness limits on our

galaxies as their work (Table 1 of Darvish et al. 2016) for a fair comparison. Figure 6 shows that the density dynamic range of the Darvish et al. (2016) data is smaller compared to our data (by ~ 4 dex), but the SFR and sSFR dynamic ranges of their galaxies are larger than our galaxies (by 1 – 2 dex each). Hence, Darvish et al. (2016) reports stronger trends than our work. The first row of Figure 6, showing SFRs from both works, suggests that both data sets follow qualitatively the same trends. An exception is that the median SFR of SIMBA increases towards $z > 3$ and the highest density bins ($\log(1 + \delta_{\text{gal}}^*) > 1$), a parameter space beyond that probed by Darvish et al. (2016). Based on Table 1 from Darvish et al. (2016), the mass completeness limit for their galaxies with redshifts higher than 1.1 is larger than $10^{9.93} M_\odot$, so their sample at high redshift ($z > 1$) just covers the most massive galaxies from our sample and is incomplete in detecting what we classify as lower mass galaxies in this work. Although there are noticeable differences in the dynamic range in median SFR between our work and Darvish et al. (2016), we find qualitatively similar trends for star formation as a function of the environment for all of our galaxies, on average.

A bump is noticeable in the SFE and molecular hydrogen mass fraction of our lower-mass galaxies ($\log \frac{M_*}{M_\odot} < 10$) at $z < 1.5$ that reside in lower-density regions in Figure 3. A previously quenched galaxy can "rejuvenate" if it experiences a merger event or accretes a lot of cold gas from an external gas reservoir. In this case, the gas content and star formation activity of the galaxy would increase after a drop caused by quenching. However, based on Lorenzon et al., in prep., the rejuvenation event among the quenched and post-starburst SIMBA galaxies is less than 10% at each redshift and is independent of environments. Therefore, the rejuvenation events cannot fully explain the detected trends in our work.

The "starvation" of satellite galaxies happens when they fall into galaxy clusters with hot intracluster medium (ICM). As a result, they are prevented from accreting enough cold gas from their surrounding which leads them to quench after finishing their gas content. This theory has been tested by van de Voort et al. (2017) using the EAGLE cosmological simulation. They study galaxies with $\log \frac{M_*}{M_\odot} > 8$ at redshifts $0 < z < 2$ with the environment defined as the local 3-dimensional number density of galaxies up to the 10th nearest neighbour. They find a strong suppression of gas accretion rate in dense environments, most effective on satellites at low redshifts. This phenomenon could partially explain the low star formation ac-

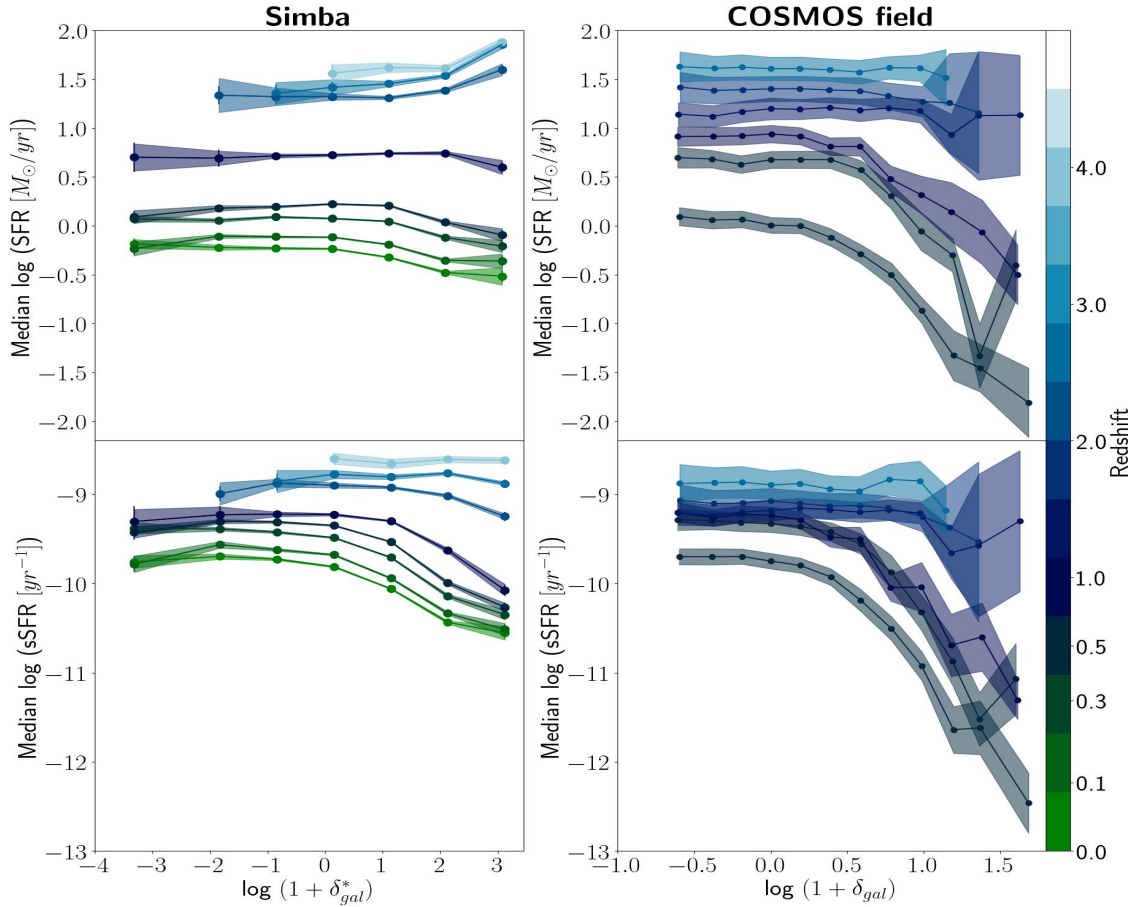


Figure 6. Comparison of the environmental dependence of star formation activity in SIMBA and the observational study based on the COSMOS survey presented in Darvish et al. (2016). Both data sets have the same stellar mass lower limits. *Left:* SFR (top) and sSFR (bottom) as functions of the environmental density at different redshifts, shown by the colour bar for SIMBA. *Right:* Same as the left column for Darvish et al. (2016) data (the right column is a reproduction of Figure 1 of Darvish et al. 2016). For visual purposes, the x-axes of the plots in the right column are more zoomed-in than the left column. SIMBA is qualitatively reproducing the observed trends in the COSMOS field, albeit SIMBA shows a smaller dynamic range in SFR and sSFR overall.

tivity of galaxies in dense regions compared to low-density regions for low-to-intermediate mass galaxies in Figure 3.

"Ram pressure stripping" is another environment-related phenomenon. When a low-mass galaxy gets bound to the gravitational field of a galaxy cluster and moves quickly in the ICM of the cluster, the pressure exerted from the hot ICM strips the gas content of the galaxy from it (Boselli et al. 2022). Darvish et al. (2018b) studies the relationship between the local environment and gas content for 708 galaxies with stellar mass $\log \frac{M_*}{M_\odot} > 10$ at $0.3 < z < 4.5$. The environment is parameterized as the environmental density calculated using the adaptive kernel smoothing method (Scoville et al. 2013) and the projected comoving distance to the 10th nearest neighbour to each galaxy for high and low redshift, respectively. This work finds no environmental dependence for gas mass fraction (defined as the ratio of the interstellar medium gas to the total gas and stellar mass) and the depletion timescale for their massive galaxies. Previous studies show that environmental-related processes like ram-pressure stripping can strip the gas content of galaxies in dense regions (Boselli & Gavazzi 2014). However, Darvish et al. (2018b) shows that ram pressure stripping is only strongly effective in galaxies with stellar mass $\log \frac{M_*}{M_\odot} < 9$ with weak gravitational potential well (Fillingham et al. 2016). As a result, ram-pressure stripping is ineffective in removing the gas content of massive galaxies, including those studied

in the work of Darvish et al. (2018b). Furthermore, molecular hydrogen (main fuel for star formation) is much denser, more bound to galaxies, and consequently less vulnerable than atomic hydrogen to be stripped from galaxies. Kenney & Young (1989) and Koyama et al. (2017) find no environmental dependence for molecular hydrogen while Fumagalli et al. (2009) finds a deficiency in molecular gas in denser environments compared to low-density environments. The stellar mass range of the galaxy sample used in Darvish et al. (2018b) is the same as the most massive galaxies we explore in SIMBA (the third row of Figure 3). We are not able to directly compare the results of these works because of the fundamental differences between the data, measurement methods, and the different definitions of galaxy properties. However, we do see a lower gas mass fraction in the two densest regions compared to lower-density regions and a small difference in SFE between the densest region and the rest of the regions. This finding is not in direct contradiction with Darvish et al. (2018b) because these dense regions of SIMBA are not explored in the observations of Darvish et al. (2018b).

Lemaux et al. (2020) investigates the reversal of the star formation-density relation using the VIMOS Ultra Deep Survey (VUDS). This work uses observations of 6730 star-forming galaxies with a stellar mass range $8 < \log \frac{M_*}{M_\odot} < 12$ and spectroscopic redshifts of $2 < z_{\text{spec}} < 5$ in three extragalactic fields of COSMOS, ECFDS,

and CFHTLS-D1 to explore the relationship between the star formation rate (SFR) of galaxies and their environmental density (δ_{gal}^*). They use the Voronoi Monte Carlo (VMC) mapping to estimate the projected density of galaxies and the environmental density contrast. In contrast to the low-redshift universe where SFR and δ_{gal}^* are anti-correlated, they find a positive correlation between these two quantities in their high-redshift sample ($2 < z < 5$). They find that this trend is mainly driven by the high fraction of massive galaxies in dense regions that are forming stars more rapidly than lower-mass galaxies. A weak but statistically significant positive correlation between SFR and δ_{gal}^* is still visible after controlling for mass and redshift dependence in this work. Although their galaxy sample and their density estimation method are different from ours, our results in the redshift range of $2 < z < 4$ are in qualitative agreement with their findings.

Wang et al. (2018) performs a similar analysis to our work on a re-simulated data set from the three hundred project³ (Cui et al. 2018). This data set includes 324 re-simulated clusters and 4 field regions from the MultiDark Planck simulation (MDPL2; Klypin et al. 2016). Wang et al. (2018) re-simulates these clusters and fields using hydrodynamical codes GADGET-X and GADGET-MUSIC. They divide their galaxies into three categories: (i) cluster galaxies are galaxies closer than $2R_{200}$ to the cluster center which is the position of the most massive dark matter halo of galaxies in each re-simulated cluster; (ii) cluster vicinity galaxies which have a distance to the cluster center between $2R_{200}$ and the fixed comoving radius of $10h^{-1}\text{Mpc}$; (iii) field galaxies within a fixed radius of $38h^{-1}\text{Mpc}$ from the center of the re-simulated field region, defined as the center of the region at $z = 0$ and fixed for all redshifts. They define the SFR of each galaxy as the sum of SFRs of all gas cells of the galaxy. The SFR of each gas cell is derived from the Springel et al. (2005) prescription. They define the environment of galaxies based on the density of all matter (dark matter, stars, and gas) calculated in a $1h^{-1}\text{Mpc}$ sphere around each galaxy and the density contrast (δ_1) is calculated compared to the average density of the universe. Their sSFR threshold to define star-forming galaxies is $\text{sSFR} > 0.3/t_{H(z)}$. Wang et al. (2018) find that for $z = 0$ star forming galaxies, sSFR declines when δ_1 increases in all of their environment categories. However, they claim this trend is driven by the high abundance of massive galaxies in dense regions. Since massive galaxies have lower sSFRs compared to low-mass galaxies, on average, they reduce the overall sSFR in dense regions. Controlling for this effect in the data, they find that the environment does not affect galaxies in cluster and cluster vicinity, but for galaxies in the field, sSFR slightly decreases when environmental density increases. We cannot directly compare these trends to our trends for SIMBA, because at $z = 0$ many galaxies in SIMBA are not star-forming based on the definition of star-forming galaxies in Wang et al. (2018). They also show that the median sSFR for all galaxies at the redshift range of $0 < z < 2.5$ falls when δ_1 increases and argue that this trend is also due to the high abundance of massive galaxies in dense regions (Figure 6 of Wang et al. 2018). The difference between the sSFR- δ_1 curves for their three environment categories (Cluster, vicinity, field) at low redshifts ($z = 0$) is much larger than those at high redshifts ($z > 1$), showing that the environment matters more at lower redshifts. Although the simulation configuration and measurement methods of this work are different from our work on SIMBA, a qualitative comparison between the trends shows that these results are broadly consistent. However, this work

has not investigated the molecular gas content and SFE, so we cannot discuss these parameters in their simulation.

Lovell et al. (2021) introduces the First Light And Reionisation Epoch Simulations (FLARES) zoom simulations and investigates the effects of the environment on the galactic properties at the epoch of reionization ($5 < z < 10$) in this simulation. Their results show a strong density dependence for the galaxy stellar mass functions and star formation rate distribution function. The galaxy star-forming main sequence, though, does not show any environmental dependence. They re-simulate spherical regions taken from a parent simulation with a box length of 3.2 comoving Gpc (Barnes et al. 2017). Using the nearest grid point mass assignment scheme, the environmental density is calculated on a ~ 2.67 comoving Mpc cubic grid. Then they find the environmental density on large scales by convolving this grid with a $14 h^{-1} \text{cMpc}$ top-hat filter and define the environmental density as $\delta(x) = \rho(x)/\bar{\rho} - 1$ where $\rho(x)$ is the dark matter density on grid points and $\bar{\rho}$ is the mean density in the box. They choose 40 regions in a way that the sample includes a number of the highest overdensities (that include the first massive galaxies) and a range of different overdensities to examine the environmental dependence of galaxy formation. The redshift ranges of the FLARES simulations investigated in Lovell et al. (2021) and SIMBA studied in our work do not overlap. Moreover, the galaxy sample used in Lovell et al. (2021) contains galaxies with stellar mass in the range of $7.5 < \log \frac{M_*}{M_\odot} < 11.3$ and $7.5 < \log \frac{M_*}{M_\odot} < 10.2$ at redshifts $z = 5$ and $z = 10$, respectively. At higher redshifts, there are fewer massive galaxies due to the hierarchical assembly of galaxies. On average, they are looking at more low-mass galaxies than our work. Furthermore, FLARES includes a larger volume than SIMBA with more abundant rare and extreme environments. Despite all these differences between these two works, it is still insightful to look at the physics behind the significant environmental trends detected in FLARES at high redshifts in contrast to SIMBA.

5.3 Caveats and future work

We are aware that several biases and limitations exist in this study. For example, hydrodynamic simulations use different theoretical prescriptions to assign galaxy properties including SFR that may not completely capture the complex physics behind the formation of galaxies. Furthermore, even the periodic simulation boxes lack a sufficient number of the largest structures in the real universe. On the other hand, the spatial resolution of simulations are limited, making it hard to capture the subgrid physics of galaxies. As a result, simulations and observations need to be used together to understand the problem in a broader view. Our work also suffers from specific caveats. We mainly explore median galaxy properties which may not represent the total distribution and scatter of all galaxies and it is not sensitive to outliers, so we might have missed some subtle variations in the distribution of galaxies. Further work is needed to check the reported trends in our work using other hydrodynamic simulations as well and confirm the physical origin of these trends.

In this work, we study the star formation activity of a large set of galaxies in a broad range of stellar mass, redshift, and environmental density. The results of this study can guide the observers to look at the galaxy sets, with specific properties, in which the environmental effects can be detected in future observational surveys. We report the most significant environmental dependences for intermediate-mass galaxies ($\log \frac{M_*}{M_\odot} < 10$) at $0 < z < 2$. Hence, observational tests of our method need an estimate of the stellar mass of galaxies up to $z = 2$ that would be feasible using the large galaxy surveys to be carried out with the James Webb Space Telescope (JWST) and

³ <https://www.nottingham.ac.uk/astronomy/The300/index.php>

the Euclid mission. It is a synergy of Euclid and JWST that will allow studying the environmental impact on physical and structural galaxy parameters introduced in Equation 10 up to $z \sim 2$. Using these parameters, observers can probe the predictions of this work.

6 SUMMARY AND CONCLUSION

In this work, we study the relationship between the star formation activity of $\sim 330,000$ simulated galaxies with stellar mass $\log \frac{M_*}{M_\odot} > 9$ and their large-scale environment from the cosmological simulation SIMBA in a redshift range of $0 < z < 4$. The environment of galaxies is defined as the environmental density of nearby galaxies, calculated on a 1 Mpc/h grid using the Cloud In Cell (CIC) method. We explore the star formation efficiency (SFE), specific star formation rate (sSFR), and molecular hydrogen mass fraction of galaxies in different redshift, stellar mass, and environmental density bins. Additionally, we fit a scaling relation for the molecular hydrogen depletion time scale as a function of redshift, specific star formation rate, stellar mass, radius, metallicity, and environmental density. Our most important findings include:

- Across the entire stellar mass range considered in this work, galaxies residing in denser regions at high redshift ($z > 1$), tend to have higher SFE than those in low-density regions. The difference is found to be ~ 0.3 dex at $z = 4$. This trend reverses around $z \sim 1$: at later cosmic times galaxies in dense regions have lower SFE than those in underdense regions, on average (~ 0.3 dex at $z = 0$).
- With a similar trend to SFE, our galaxy sample across the entire considered stellar mass range shows a weak reversal of sSFR-density relation with a turning point around $z \sim 2.5$.
- Controlling for stellar mass variation, at low redshift ($z < 1$), the low to intermediate mass galaxies ($9 < \log \frac{M_*}{M_\odot} < 10$) in dense regions have lower SFE and sSFR than galaxies in underdense regions. The molecular hydrogen mass fraction is lower in dense regions compared to low-density regions for all galaxies regardless of their stellar mass and redshift.
- We provide a scaling relation to determine depletion timescales (and therefore SFE) in galaxies at $0 < z < 4$ with $\log \frac{M_*}{M_\odot} > 9$. The proposed model takes into account the environmental density parameter, which is found to be a statistically important term in the fit.

ACKNOWLEDGEMENTS

We warmly acknowledge Behnam Darvish for providing us with their data and Sara Ellison for her thoughtful comments and discussions. DD. acknowledges support from the National Science Center (NCN) starting grant SONATA (UMO-2020/39/D/ST9/00720). LG. and AWSM. acknowledge the support of the Natural Sciences and Engineering Research Council of Canada (NSERC) through grant reference number RGPIN-2021-03046.

DATA AVAILABILITY

The galaxy catalogues used in this work are available at the SIMBA project repository⁴. The full tables including the environment measurements are available upon request.

⁴ <http://simba.roe.ac.uk/>

REFERENCES

- Alberts S., Adams J., Gregg B., Pope A., Williams C. C., Eisenhardt P. R. M., 2022, *ApJ*, **927**, 235
- Anglés-Alcázar D., Davé R., Faucher-Giguère C.-A., Özel F., Hopkins P. F., 2017a, *MNRAS*, **464**, 2840
- Anglés-Alcázar D., Faucher-Giguère C.-A., Kereš D., Hopkins P. F., Quataert E., Murray N., 2017b, *MNRAS*, **470**, 4698
- Appleby S., Davé R., Sorini D., Storey-Fisher K., Smith B., 2021, *MNRAS*, **507**, 2383
- Bahé Y. M., et al., 2017, *MNRAS*, **470**, 4186
- Balogh M., et al., 2004, *MNRAS*, **348**, 1355
- Bamford S. P., et al., 2009, *MNRAS*, **393**, 1324
- Barnes D. J., Kay S. T., Henson M. A., McCarthy I. G., Schaye J., Jenkins A., 2017, *MNRAS*, **465**, 213
- Bernardi M., Meert A., Sheth R. K., Fischer J.-L., Huertas-Company M., Maraston C., Shankar F., Vikram V., 2017, *Monthly Notices of the Royal Astronomical Society*, p. stx176
- Berrier H. D., Barton E. J., Berrier J. C., Bullock J. S., Zentner A. R., Wechsler R. H., 2011, *ApJ*, **726**, 1
- Birdsall C. K., Fuss D., 1969, *Journal of Computational Physics*, **3**, 494
- Bolzonella M., et al., 2010, *A&A*, **524**, A76
- Bondi H., 1952, *MNRAS*, **112**, 195
- Boselli A., Gavazzi G., 2014, *A&ARv*, **22**, 74
- Boselli A., Gavazzi G., Donas J., Scodreggio M., 2001, *AJ*, **121**, 753
- Boselli A., Cortese L., Boquien M., Boissier S., Catinella B., Lagos C., Saintonge A., 2014, *A&A*, **564**, A66
- Boselli A., Fossati M., Sun M., 2022, *A&ARv*, **30**, 3
- Calabrò A., et al., 2022, *A&A*, **664**, A75
- Chartab N., et al., 2021, *ApJ*, **908**, 120
- Choi E., Ostriker J. P., Naab T., Johansson P. H., 2012, *ApJ*, **754**, 125
- Conroy C., Dutton A. A., Graves G. J., Mendel J. T., van Dokkum P. G., 2013, *The Astrophysical Journal*, **776**, L26
- Cooper M. C., et al., 2008, *MNRAS*, **383**, 1058
- Cui W., et al., 2018, *MNRAS*, **480**, 2898
- Darvish B., Mobasher B., Sobral D., Scoville N., Aragon-Calvo M., 2015, *ApJ*, **805**, 121
- Darvish B., Mobasher B., Sobral D., Rettura A., Scoville N., Faisst A., Capak P., 2016, *ApJ*, **825**, 113
- Darvish B., Martin C., Gonçalves T. S., Mobasher B., Scoville N. Z., Sobral D., 2018a, *ApJ*, **853**, 155
- Darvish B., Scoville N. Z., Martin C., Mobasher B., Diaz-Santos T., Shen L., 2018b, *ApJ*, **860**, 111
- Davé R., Crain R. A., Stevens A. R. H., Narayanan D., Saintonge A., Catinella B., Cortese L., 2020, *MNRAS*, **497**, 146
- Davé R., Thompson R., Hopkins P. F., 2016, *Monthly Notices of the Royal Astronomical Society*, **462**, 3265
- Davé R., Anglés-Alcázar D., Narayanan D., Li Q., Rafieferantsoa M. H., Appleby S., 2019, *Monthly Notices of the Royal Astronomical Society*, **486**, 2827–2849
- Dressler A., 1980, *ApJ*, **236**, 351
- Duivenvoorden S., et al., 2016, *MNRAS*, **462**, 277
- Elbaz D., et al., 2007, *Astronomy & Astrophysics*, **468**, 33–48
- Ellison S. L., Patton D. R., Simard L., McConnachie A. W., Baldry I. K., Mendel J. T., 2010, *MNRAS*, **407**, 1514
- Etherington J., Thomas D., 2015, *MNRAS*, **451**, 660
- Fillingham S. P., Cooper M. C., Pace A. B., Boylan-Kolchin M., Bullock J. S., Garrison-Kimmel S., Wheeler C., 2016, *MNRAS*, **463**, 1916
- Fumagalli M., Krumholz M. R., Prochaska J. X., Gavazzi G., Boselli A., 2009, *ApJ*, **697**, 1811
- Goto T., Yamauchi C., Fujita Y., Okamura S., Sekiguchi M., Smail I., Bernardi M., Gomez P. L., 2003, *Monthly Notices of the Royal Astronomical Society*, **346**, 601
- Haas M. R., Schaye J., Jeesson-Daniel A., 2012, *MNRAS*, **419**, 2133
- Hahn O., Porciani C., Carollo C. M., Dekel A., 2007, *MNRAS*, **375**, 489
- Hayashi M., et al., 2018, *ApJ*, **856**, 118
- Hopkins P. F., 2015, *Monthly Notices of the Royal Astronomical Society*, **450**, 53

- Hopkins P. F., Quataert E., 2011, *MNRAS*, **415**, 1027
- Hopkins P. F., Kereš D., Oñorbe J., Faucher-Giguère C.-A., Quataert E., Murray N., Bullock J. S., 2014, *MNRAS*, **445**, 581
- Hunt L., Dayal P., Magrini L., Ferrara A., 2016, *MNRAS*, **463**, 2020
- Hwang H. S., Shin J., Song H., 2019, *MNRAS*, **489**, 339
- Ito K., et al., 2023, *ApJ*, **945**, L9
- Kaiser N., 1987, *MNRAS*, **227**, 1
- Kauffmann G., White S. D. M., Heckman T. M., Ménard B., Brinchmann J., Charlot S., Tremonti C., Brinkmann J., 2004, *MNRAS*, **353**, 713
- Kenney J. D. P., Young J. S., 1989, *ApJ*, **344**, 171
- Klypin A., Yepes G., Gottlöber S., Prada F., Heß S., 2016, *MNRAS*, **457**, 4340
- Koyama S., et al., 2017, *ApJ*, **847**, 137
- Krumholz M. R., Dekel A., 2012, *ApJ*, **753**, 16
- Krumholz M. R., Gnedin N. Y., 2011, *The Astrophysical Journal*, **729**, 36
- Lavezzi T. E., Dickey J. M., 1998, *The Astronomical Journal*, **115**, 405
- Lee M. M., et al., 2017, *ApJ*, **842**, 55
- Lemaux B. C., et al., 2020, The VIMOS Ultra Deep Survey: The Reversal of the Star Formation Rate – Density Relation at $2 < z < 5$ ([arXiv:2009.03324](https://arxiv.org/abs/2009.03324))
- Liu D., et al., 2019, *ApJ*, **887**, 235
- Lovell C. C., Thomas P. A., Wilkins S. M., 2018, *MNRAS*, **474**, 4612
- Lovell C. C., Vijayan A. P., Thomas P. A., Wilkins S. M., Barnes D. J., Irodotou D., Roper W., 2021, *MNRAS*, **500**, 2127
- Lu A., et al., 2022, *MNRAS*,
- McConachie I., et al., 2022, *ApJ*, **926**, 37
- Mei S., et al., 2023, *A&A*, **670**, A58
- Mo H. J., White S. D. M., 1996, *MNRAS*, **282**, 347
- Mok A., et al., 2016, *MNRAS*, **456**, 4384
- Moorman C. M., Moreno J., White A., Vogeley M. S., Hoyle F., Giovanelli R., Haynes M. P., 2016, *ApJ*, **831**, 118
- Muldrew S. I., et al., 2012, *MNRAS*, **419**, 2670
- Muldrew S. I., Hatch N. A., Cooke E. A., 2015, *MNRAS*, **452**, 2528
- Noble A. G., et al., 2017, *ApJ*, **842**, L21
- Old L. J., et al., 2020, *Monthly Notices of the Royal Astronomical Society*, **493**, 5987
- Patel S. G., Holden B. P., Kelson D. D., Illingworth G. D., Franx M., 2009, *ApJ*, **705**, L67
- Peng Y.-j., et al., 2010, *ApJ*, **721**, 193
- Peng Y.-j., Lilly S. J., Renzini A., Carollo M., 2012, *ApJ*, **757**, 4
- Planck Collaboration et al., 2016, *A&A*, **594**, A13
- Popesso P., et al., 2015, *Astronomy & Astrophysics*, **574**, A105
- Robert C. Kennicutt J., 1998, *The Astrophysical Journal*, **498**, 541
- Rodríguez Montero F., Davé R., Wild V., Anglés-Alcázar D., Narayanan D., 2019, *MNRAS*, **490**, 2139
- Santos J. S., et al., 2014, *MNRAS*, **438**, 2565
- Santos J. S., et al., 2015, *MNRAS*, **447**, L65
- Schaye J., et al., 2015, *MNRAS*, **446**, 521
- Schmidt M., 1959, *ApJ*, **129**, 243
- Scott T. C., Usero A., Brinks E., Boselli A., Cortese L., Bravo-Alfaro H., 2013, *MNRAS*, **429**, 221
- Scoville N., et al., 2013, *ApJS*, **206**, 3
- Scoville N., et al., 2017, *ApJ*, **837**, 150
- Shimakawa R., et al., 2018, *MNRAS*, **473**, 1977
- Skibba R. A., et al., 2009, *MNRAS*, **399**, 966
- Smolčić V., et al., 2017, *A&A*, **597**, A4
- Sobolev V. V., 1960, *Moving Envelopes of Stars*, [doi:10.4159/harvard.9780674864658](https://doi.org/10.4159/harvard.9780674864658).
- Song M., et al., 2016, *The Astrophysical Journal*, **825**, 5
- Speagle J. S., Steinhardt C. L., Capak P. L., Silverman J. D., 2014, *ApJS*, **214**, 15
- Springel V., et al., 2005, *Nature*, **435**, 629
- Tacconi L. J., et al., 2018, *The Astrophysical Journal*, **853**, 179
- Tadaki K.-i., et al., 2019, *PASJ*, **71**, 40
- Thomas N., Davé R., Anglés-Alcázar D., Jarvis M., 2019, *MNRAS*, **487**, 5764
- Tomczak A. R., et al., 2014, *The Astrophysical Journal*, **783**, 85
- Tonnesen S., Cen R., 2014, *ApJ*, **788**, 133
- Villaescusa-Navarro F., et al., 2018, *ApJ*, **866**, 135
- Vulcani B., et al., 2013, *A&A*, **550**, A58
- Wang Y., et al., 2018, *ApJ*, **868**, 130
- Woo J., et al., 2013, *MNRAS*, **428**, 3306
- Wu J. F., 2020, *ApJ*, **900**, 142
- Xu W., et al., 2020, *MNRAS*, **498**, 1839
- Yajima H., et al., 2022, *MNRAS*, **509**, 4037
- Young J. S., Allen L., Kenney J. D. P., Lesser A., Rownd B., 1996, *AJ*, **112**, 1903
- Zavala J. A., et al., 2019, *ApJ*, **887**, 183
- van de Voort F., Bahé Y. M., Bower R. G., Correa C. A., Crain R. A., Schaye J., Theuns T., 2017, *MNRAS*, **466**, 3460
- van der Wel A., et al., 2014, *The Astrophysical Journal*, **788**, 28

APPENDIX A: TABLES

Table A1 shows the binning of galaxies based on stellar mass, redshift, and overdensity, used in Figure 3. Table A2 shows the properties of the models we fitted for the molecular gas depletion time of galaxies in Section 4.3.

This paper has been typeset from a $\mathrm{\LaTeX}$ file prepared by the author.

Table A1. The number of galaxies in each bin specified by stellar mass, redshift, and the stellar mass overdensity.

9 < log M^*/M_\odot < 9.5						9.5 < log M^*/M_\odot < 10						10 < log M^*/M_\odot					
z	log 1 + δ	N	z	log 1 + δ	N	z	log 1 + δ	N	z	log 1 + δ	N	z	log 1 + δ	N	z	log 1 + δ	N
0.0	-1.62	794	1.9	-1.62	817	0.0	-1.62	667	1.9	-1.62	223	0.0	-1.62	163	1.9	-1.62	62
	-0.69	2511		-0.69	1906		-0.69	2677		-0.69	780		-0.69	919		-0.69	363
	0.23	4025		0.23	2047		0.23	5572		0.23	1304		0.23	3248		0.23	1140
	1.16	2118		1.16	1239		1.16	2640		1.16	709		1.16	2528		1.16	1161
	2.09	60		2.09	276		2.09	64		2.09	156		2.09	73		2.09	290
0.1	-1.62	794	2.0	-1.62	756	0.1	-1.62	640	2.0	-1.62	191	0.1	-1.62	170	2.0	-1.62	43
	-0.69	2356		-0.69	1874		-0.69	2528		-0.69	685		-0.69	982		-0.69	299
	0.23	3738		0.23	2036		0.23	5158		0.23	1177		0.23	3437		0.23	1018
	1.16	2120		1.16	1210		1.16	2512		1.16	657		1.16	2728		1.16	1035
	2.09	57		2.09	268		2.09	63		2.09	145		2.09	72		2.09	290
0.3	-1.62	752	2.2	-1.62	713	0.3	-1.62	546	2.2	-1.62	133	0.3	-1.62	191	2.2	-1.62	47
	-0.69	2043		-0.69	1808		-0.69	2234		-0.69	608		-0.69	1082		-0.69	246
	0.23	3336		0.23	2047		0.23	4385		0.23	1084		0.23	3734		0.23	864
	1.16	1881		1.16	1141		1.16	2208		1.16	577		1.16	2762		1.16	886
	2.09	87		2.09	282		2.09	94		2.09	170		2.09	135		2.09	264
0.5	-1.62	817	2.4	-1.62	637	0.5	-1.62	505	2.4	-1.62	122	0.5	-1.62	240	2.4	-1.62	34
	-0.69	1944		-0.69	1676		-0.69	1937		-0.69	452		-0.69	1121		-0.69	167
	0.23	3041		0.23	2088		0.23	3546		0.23	1074		0.23	3683		0.23	635
	1.16	1820		1.16	1040		1.16	2001		1.16	503		1.16	2859		1.16	713
	2.09	81		2.09	271		2.09	90		2.09	163		2.09	170		2.09	224
0.7	-1.62	755	2.5	-1.62	583	0.7	-1.62	446	2.5	-1.62	100	0.7	-1.62	203	2.5	-1.62	21
	-0.69	1850		-0.69	1640		-0.69	1638		-0.69	399		-0.69	1099		-0.69	153
	0.23	2883		0.23	2017		0.23	2940		0.23	1034		0.23	3445		0.23	538
	1.16	1725		1.16	988		1.16	1631		1.16	494		1.16	2789		1.16	606
	2.09	107		2.09	286		2.09	104		2.09	154		2.09	187		2.09	231
0.8	-1.62	741	2.7	-1.62	494	0.8	-1.62	421	2.7	-1.62	91	0.8	-1.62	201	2.7	-1.62	8
	-0.69	1876		-0.69	1532		-0.69	1499		-0.69	361		-0.69	1022		-0.69	115
	0.23	2773		0.23	2033		0.23	2679		0.23	917		0.23	3324		0.23	424
	1.16	1666		1.16	945		1.16	1459		1.16	456		1.16	2637		1.16	535
	2.09	143		2.09	287		2.09	120		2.09	137		2.09	246		2.09	194
1.0	-1.62	839	3.0	-1.62	465	1.0	-1.62	385	3.0	-1.62	87	1.0	-1.62	219	3.0	-1.62	11
	-0.69	1859		-0.69	1385		-0.69	1285		-0.69	284		-0.69	880		-0.69	80
	0.23	2562		0.23	2077		0.23	2161		0.23	739		0.23	2756		0.23	300
	1.16	1751		1.16	961		1.16	1369		1.16	453		1.16	2476		1.16	444
	2.09	148		2.09	275		2.09	118		2.09	121		2.09	267		2.09	161
1.2	-1.62	857	3.2	-1.62	432	1.2	-1.62	327	3.2	-1.62	65	1.2	-1.62	186	3.2	-1.62	14
	-0.69	1925		-0.69	1263		-0.69	1132		-0.69	251		-0.69	770		-0.69	56
	0.23	2378		0.23	2145		0.23	1856		0.23	660		0.23	2344		0.23	237
	1.16	1626		1.16	958		1.16	1171		1.16	422		1.16	2022		1.16	344
	2.09	200		2.09	259		2.09	130		2.09	106		2.09	273		2.09	147
1.4	-1.62	754	3.5	-1.62	366	1.4	-1.62	309	3.5	-1.62	43	1.4	-1.62	141	3.5	-1.62	13
	-0.69	1987		-0.69	1127		-0.69	1052		-0.69	186		-0.69	667		-0.69	32
	0.23	2275		0.23	2102		0.23	1647		0.23	547		0.23	1972		0.23	147
	1.16	1531		1.16	986		1.16	1010		1.16	443		1.16	1838		1.16	294
	2.09	261		2.09	230		2.09	135		2.09	94		2.09	313		2.09	118
1.5	-1.62	782	3.7	-1.62	312	1.5	-1.62	278	3.7	-1.62	36	1.5	-1.62	111	3.7	-1.62	11
	-0.69	1965		-0.69	1037		-0.69	975		-0.69	165		-0.69	597		-0.69	27
	0.23	2201		0.23	2033		0.23	1588		0.23	479		0.23	1719		0.23	107
	1.16	1461		1.16	971		1.16	921		1.16	424		1.16	1658		1.16	248
	2.09	273		2.09	217		2.09	151		2.09	91		2.09	353		2.09	114
1.7	-1.62	765	4.0	-1.62	255	1.7	-1.62	258	4.0	-1.62	25	1.7	-1.62	88	4.0	-1.62	6
	-0.69	2010		-0.69	849		-0.69	883		-0.69	126		-0.69	466		-0.69	25
	0.23	2160		0.23	1794		0.23	1414		0.23	388		0.23	1338		0.23	71
	1.16	1308		1.16	945		1.16	821		1.16	404		1.16	1372		1.16	174
	2.09	281		2.09	235		2.09	166		2.09	92		2.09	315		2.09	99

Table A2. Different models fitted to the depletion time of galaxies as functions of redshift, stellar mass, specific star formation rate, stellar mass overdensity, metallicity, and galaxy size with this equation: $\log t_{\text{depl}} (\text{Gyr}) = A + B \log(1+z) + C \log sSFR + D \log M_* + E \log(R) + F \log(Z) + G \log(1+\delta)$

Model	Variable	Coefficient	STD	Conf.int	P-value	Model	Variable	Coefficient	STD	Conf.int	P-value
Model 1 $R^2 =$ 0.833259	Const. 1+z δMS M_* $R_h/Re0$	0.672 -2.11 -0.433 -0.04 0.82	0.005 0.002 0.0 0.001 0.001	[0.662, 0.683] [-2.114, -2.106] [-0.434, -0.432] [-0.041, -0.039] [0.818, 0.823]	0.0 0.0 0.0 0.0 0.0	Model 6 $R^2 =$ 0.833295	Const. 1+z δMS M_* $R_h/Re0$ Z	0.576 -2.113 -0.437 -0.033 0.808 -0.015	0.013 0.002 0.001 0.001 0.002 0.002	[0.552, 0.601] [-2.118, -2.109] [-0.438, -0.435] [-0.035, -0.032] [0.804, 0.812] [-0.019, -0.012]	0.0 0.0 0.0 0.0 0.0 2.5×10^{-17}
Model 2 $R^2 =$ 0.833369	Const. 1+z δMS M_* $R_h/Re0$ $1 + \delta$	0.692 -2.112 -0.432 -0.042 0.821 0.004	0.006 0.002 0.0 0.001 0.001 0.0	[0.681, 0.703] [-2.117, -2.108] [-0.433, -0.432] [-0.043, -0.041] [0.818, 0.824] [0.004, 0.005]	0.0 0.0 0.0 0.0 0.0 0.0	Model 7 $R^2 =$ 0.833413	Const. 1+z δMS M_* $R_h/Re0$ Z $1 + \delta$	0.586 -2.116 -0.437 -0.035 0.808 -0.017 0.005	0.013 0.002 0.001 0.001 0.002 0.002 0.000	[0.561, 0.611] [-2.12, -2.112] [-0.438, -0.435] [-0.037, -0.033] [0.804, 0.812] [-0.021, -0.013] [0.004, 0.005]	0.0 0.0 0.0 0.0 0.0 2.1×10^{-27} 0.0
Model 3 $R^2 =$ 0.865279	Const. 1+z sSFR M_* $R_h/Re0$ $1 + \delta$	-2.346 -1.036 -0.433 -0.168 0.837 0.002	0.005 0.002 0.0 0.001 0.001 0.0	[-2.356, -2.335] [-1.04, -1.031] [-0.433, -0.432] [-0.169, -0.167] [0.834, 0.839] [0.001, 0.002]	0.0 0.0 0.0 0.0 0.0 4.3×10^{-13}	Model 8 $R^2 =$ 0.866192	Const. 1+z sSFR M_* $R_h/Re0$ Z $1 + \delta$	-2.954 -1.009 -0.450 -0.141 0.775 -0.078 0.002	0.014 0.002 0.001 0.001 0.002 0.002 0.000	[-2.981, -2.927] [-1.013, -1.004] [-0.451, -0.449] [-0.143, -0.14] [0.772, 0.779] [-0.081, -0.075] [0.002, 0.003]	0.0 0.0 0.0 0.0 0.0 0.0 2.8×10^{-24}
Model 4 $R^2 =$ 0.833369	Const. 1+z δMS M_* R_h $1 + \delta$	1.933 -1.496 -0.432 -0.231 0.821 0.004	0.005 0.002 0.0 0.001 0.001 0.0	[1.922, 1.944] [-1.499, -1.493] [-0.433, -0.432] [-0.232, -0.229] [0.818, 0.824] [0.004, 0.005]	0.0 0.0 0.0 0.0 0.0 0.0	Model 9 $R^2 =$ 0.833413	Const. 1+z δMS M_* R_h Z $1 + \delta$	1.807 -1.510 -0.437 -0.220 0.808 -0.017 0.005	0.015 0.002 0.001 0.001 0.002 0.002 0.000	[1.778, 1.835] [-1.515, -1.506] [-0.438, -0.435] [-0.223, -0.218] [0.804, 0.812] [-0.021, -0.013] [0.004, 0.005]	0.0 0.0 0.0 0.0 0.0 2.1×10^{-27} 0.0
Model 5 $R^2 =$ 0.865279	Const. 1+z sSFR M_* R_h $1 + \delta$	-1.081 -0.408 -0.433 -0.36 0.837 0.002	0.005 0.002 0.0 0.001 0.001 0.0	[-1.092, -1.07] [-0.412, -0.405] [-0.433, -0.432] [-0.361, -0.359] [0.834, 0.839] [0.001, 0.002]	0.0 0.0 0.0 0.0 0.0 4.3×10^{-13}	Model10 $R^2 =$ 0.866192	Const. 1+z sSFR M_* R_h Z $1 + \delta$	-1.782 -0.427 -0.450 -0.319 0.775 -0.078 0.002	0.016 0.002 0.001 0.001 0.002 0.002 0.000	[-1.813, -1.751] [-0.43, -0.424] [-0.451, -0.449] [-0.321, -0.318] [0.772, 0.779] [-0.081, -0.075] [0.002, 0.003]	0.0 0.0 0.0 0.0 0.0 0.0 2.8×10^{-24}